Exploring sources of gravity waves in the southern winter stratosphere through ray-tracing 3-D satellite observations

Phoebe E. Noble[1,2], Sebastian Rhode[3,5], Neil P. Hindley[1], Peter Berthelemy[1,2], Tracy Moffat-Griffin[2], Peter Preusse[3,5], Lars Hoffmann[4,5], Corwin J. Wright[1]

[1]Centre for Climate Adaptation & Environment Research, Department of Electronic Engineering, University of Bath, Bath, UK
[2]Atmosphere, Ice and Climate Team, British Antarctic Survey, Cambridge, UK
[3]Institute of Energy and Climate Research, Stratosphere (IEK-7), Forschungszentrum Jülich, Jülich, Germany
[4]Jülich Supercomputing Center (JSC), Forschungszentrum Jülich, Jülich, Germany
[5]Center for Advanced Simulation and Analytics (CASA), Forschungszentrum Jülich, Jülich, Germany

Key Points:

- Ray-tracing reveals that gravity waves observed at all longitudes around the Southern Ocean converge to 60°S as they propagate upwards.
- We quantify the momentum flux from different regions, finding that, in winter, 56% of momentum flux is traced back to ocean and 44% to land.
- Small island sources in the Southern Ocean contribute disproportionately to the total observed momentum flux.

Corresponding author: Phoebe Noble, `pn399@bath.ac.uk`

Abstract

During winter, the latitude belt at 60°S is one of the most intense hotspots of stratospheric gravity wave (GW) activity. However, producing accurate representations of GW dynamics in this region in numerical models has proved exceptionally challenging. One reason for this is that questions remain regarding the relative contributions of different orographic and non-orographic sources of GWs here.

We use 3-D satellite GW observations from the Atmospheric InfraRed Sounder (AIRS) from winter 2012 in combination with the Gravity-wave Regional Or Global Ray Tracer (GROGRAT) to backwards ray trace GWs to their sources. We trace over 14.2 million rays, which allows us to investigate GW propagation and to produce systematic estimates of the relative contribution of orographic and non-orographic sources to the total observed stratospheric GW momentum flux in this region.

We find that in winter 56% of momentum flux (MF) traces back to the ocean and 44% to land, despite land representing less than a quarter of the region's area. This demonstrates that, while orographic sources contribute much more momentum flux per unit area, the large spatial extent of non-orographic sources leads to a higher overall contribution. The small islands of Kerguelen and South Georgia specifically contribute up to 1.6% and 0.7% of average monthly stratospheric MF, and the intermittency of these sources suggests that their short-timescale contribution is even higher. These results provide the important insights needed to significantly advance our knowledge of the atmospheric momentum budget in the Southern polar region.

Plain Language Summary

Just like the ocean, our atmosphere contains waves which transport energy and momentum. These atmospheric waves, known as gravity waves (GWs), strongly influence large-scale wind patterns but are hard to represent in weather and climate models. The Southern Hemispheric stratosphere has some of the strongest GW activity on our planet and accurately representing this region in models has proved exceptionally challenging. Further, the exact contributions of GWs from different sources, such as flow over mountains, convection in storms and weather systems, and instabilities in the atmospheric flow, are large unknowns that can lead to major model biases.

Here, we use satellite observations of stratospheric GWs and, using new methods, separate GW observations from noise and measure GW amplitudes, wavelengths and directions. We then use these observations in combination with a ray tracing model to track observed GWs back to their sources near the ground. We trace more than 14.2 million observed GW events. This approach means that for the first time we are able to produce systematic estimates of the relative contribution of different wave sources to the observed stratospheric activity in this region.

1 Introduction

Gravity waves (GWs) are small-scale buoyancy waves in the atmosphere for which gravity/buoyancy acts as a restoring force. These waves play a major role in the vertical coupling of the atmosphere, transporting momentum and driving the circulation at high altitudes, in particular the overarching mesospheric circulation branch (Fritts & Alexander, 2003). Misrepresentation of GWs in General Circulation Models (GCMs) can lead to major circulation biases.

During winter, the southern hemispheric polar stratosphere is the world's strongest region of GW activity (Hoffmann et al. (2013); Hindley et al. (2020, 2015); Wright et al. (2016); Bacmeister and Schoeberl (1989); Alexander et al. (2010); Hertzog et al. (2012) and many others). Here, maps of GW activity are dominated by orographic waves from the Southern Andes and Antarctic Peninsula, where strong surface winds flow perpendicularly over tall mountains, forcing air upwards and generating the highest-amplitude stratospheric GWs on Earth. Small islands such as South Georgia (Hindley et al., 2020) and Kerguelen (Alexander & Grimsdell, 2013) spread across the Southern Ocean also act as strong local sources (Hoffmann et al., 2016), generating GW tails which stretch hundreds of kilometres downstream (Alexander et al., 2009). Additionally, intense GW activity is found all around the 60°S belt over open ocean and is believed to be generated by non-orographic sources such as storms, frontogenesis and jet adjustment processes around the edge of the polar vortex (Wu & Eckermann, 2008; Holt et al., 2017, 2023; Hendricks et al., 2014; Plougonven et al., 2017; Hindley et al., 2015; Strube et al., 2021). Consistently strong wind conditions that increase with altitude during winter allow GWs generated in the lower atmosphere to propagate upwards through the stratosphere, where their momentum deposition can have a major impact on the global general circulation by decelerating the background winds.

Most weather and climate models use simplified representations of GWs, and this can have significant and negative consequences. For example, it is widely hypothesised that missing GW drag in models is a leading-order mechanism underlying the 'cold pole' bias (McLandress et al., 2011; Holt et al., 2023; Alexander & Grimsdell, 2013), whereby the Southern Hemisphere polar stratosphere is too cold in winter and the polar stratospheric vortex breaks down too late in spring relative to observations. Supporting this hypothesis, models persistently show a significant local reduction in stratospheric GW momentum flux (MF) at 60°S in disagreement with observations (Holt et al., 2023; Geller et al., 2013).

While the community agrees that the cold pole problem bias is primarily due to missing GW drag, the source of the GWs that produce this drag remains a topic of major debate. Previous studies suggest that at least a proportion of the missing flux can be explained by the lateral convergence of GWs from sources poleward and equatorward of 60°S. This has been demonstrated in model ray-tracing experiments by Sato et al. (2011); Rhode et al. (2023) and shown to be consistent observed directional GW properties by Wright et al. (2017), Hindley et al. (2015) and Moffat-Griffin et al. (2020).

Other work, meanwhile, highlights underrepresented orographic MF from small islands in the Southern Ocean as a possible source. In NASA's Goddard Earth Observing System Chemistry Climate Model (GEOS CCM), Garfinkel and Oman (2018) increased the orographic wave drag over three small islands in the Southern Ocean to near observed levels and found a reduction in the cold pole bias. Observationally, meanwhile, Hoffmann et al. (2016) explored GW activity from 18 hotspots including small islands in the Southern Ocean using AIRS satellite data, and concluded that mountain waves at these hotspots contribute significantly to overall observed MF. MF from these small islands is often vastly underestimated in models as the island size is much smaller than the model grid cell (Alexander et al., 2009). Finally, research has highlighted the importance of non-orographic GWs, which can be generated across the large spatial area of the Southern Ocean and may hence integrate to make a large overall contribution to total MF at these latitudes (Plougonven et al., 2013; Hertzog et al., 2008; Jewtoukoff et al., 2015; Plougonven et al., 2020).

Garcia et al. (2017) explored the modification of the Whole Atmosphere Community Climate Model (WACCM)'s GW parametrisation and noted that increasing orographic GW forcing reduced the cold pole bias, but that other approaches to enhance GW activity can also reduce the bias. For example, recently, Eichinger et al. (2023) found a reduction in model biases by implementing a parametrisation that included lateral propagation. This highlights the need for observational work to determine the specific behaviour of the real atmosphere. Untangling the sources of GWs in this region, their relative importance and their propagation behaviour could provide a key way to address this knowledge gap. This would in turn help advance weather and climate modelling, reduce the cold pole bias and simultaneously address many other problems arising in this region from the poor simulation of GW effects.

Ray-tracing methods provide an ideal tool for tackling this problem and have consequently been employed previously in various GW studies. Ray-tracing is a technique whereby GWs with specified initial conditions are propagated through a background atmosphere in time. Previous forward-tracing work has used model-derived (for instance Preusse et al., 2014; Sato et al., 2011; Vosper, 2015), observationally determined (Preusse et al., 2009; Krasauskas et al., 2023; Pramitha et al., 2020) or idealised (Alexander, 1998; Q. Jiang et al., 2019; Preusse et al., 2002) GW properties to launch GW from locations on the surface and explore their propagation through model/reanalysis background fields. Backwards ray-tracing, where GW properties are defined later in the GW's lifecycle, such as from observations, allows for the determination of GW sources. Pulido et al. (2013) backwards ray-traced radiosonde observations from a case study over the Andes and Wrasse et al. (2006) backwards ray-traced airglow observations from four mid-latitude sites. Krisch et al. (2017) used observations of a gravity wave event over Iceland from the aircraft based Gimballed Limb Observer for Radiance Imaging of the Atmosphere (GLORIA) and traced the waves forwards and backwards from 11.5 km altitude. More recently, Perrett et al. (2020) backwards traced a single month of AIRS observations in the Southern Hemisphere, providing a proof of concept we expand upon in this study.

Backwards tracing stratospheric AIRS observations is a particularly powerful method for untangling GW source mechanisms in this region. The observed 3-D wave vector is fully characterised by using a 3-D AIRS retrieval and the recently developed 3-D spectral analysis technique which allows for full 3-D inputs for ray-tracing. Additionally, our use of satellite data as the input for back-tracing allows for spatial coverage that ground-based or radiosonde observations cannot achieve. This specifically allows us to explore (i) convergence of GWs to 60°S, (ii) downstream propagation of orographic GWs, (iii) spatial distribution of MF from orographic and non-orographic sources, (iv) quantifying MF originating from different source regions across the southern polar region.

We present the Data in Section 2, Section 3 describes the methods used to obtain GW properties and perform the ray tracing. Results are presented and discussed in Section 4 and we conclude our work in Section 5.

2 Data

2.1 3-D gravity wave observations from AIRS

We use stratospheric GW observations made in polar winter from May to September 2012 by the Atmospheric InfraRed Sounder (AIRS) onboard the National Aeronautics and Space Administration's (NASA) Aqua satellite (Aumann et al., 2003; Chahine et al., 2006). Aqua was launched in 2002 and is still operating. We chose 2012 for this work as it was a non-extreme year for the Quasi-biennial Oscillation (QBO) and the El Niño Southern Oscillation (ENSO), and as such we expect it to be a broadly representative year.

Aqua follows a near-polar orbit with a period of ≈ 100 minutes. AIRS is a hyperspectral imager and measures atmospheric radiances in a cross-track sampling geometry. The data have a swath width of 1 780 km with a resolution of 13.5 km (across-track) x 18 km (along-track) at the nadir, which reduces towards the edges of the swath (Hoffmann et al., 2014). We use the 3-D temperature retrieval of Hoffmann and Alexander (2009); this retrieval covers a height range of 20 to 60 km and uses the instrument's full sampling resolution to enhance the horizontal resolution by a factor of three compared to the operational retrieval.

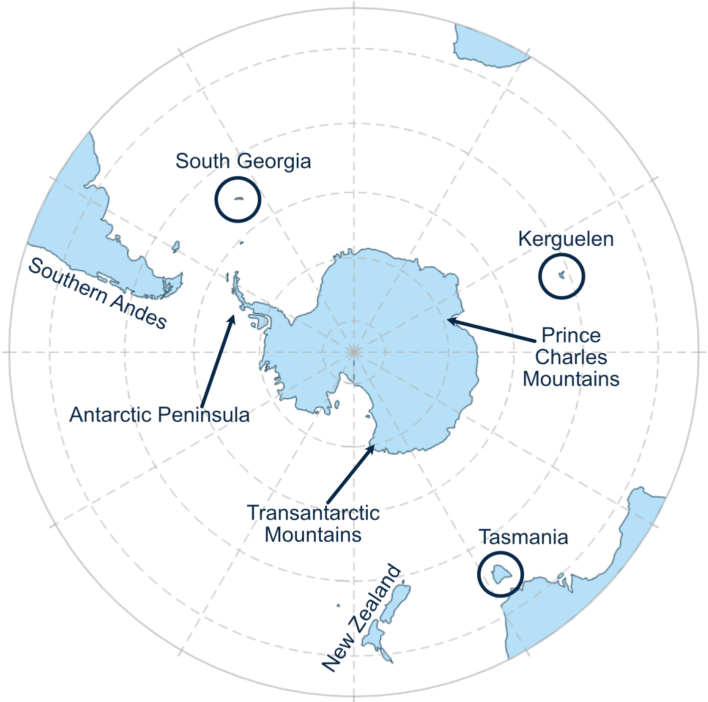

Figure 1. The Southern Hemisphere study region

No single measurement technique can observe the full spectrum of GWs, and observations will be sensitive to specific scales depending on observational and methodological characteristics; this issue is known as the observational filter. The observational filter of different observational techniques for measuring GWs is described in more detail by Alexander et al. (2010) and Wright et al. (2016). Hindley et al. (2019) investigated the observational filter of AIRS by characterising the sensitivity of the Hoffmann and Alexander (2009) retrieval. The retrieval was found to be almost 100% sensitive to GWs with vertical wavelengths between 35-45km and horizontal wavelengths less than 500km. However, this sensitivity fell with decreasing vertical wavelength and increasing horizontal wavelength. For example, wavelengths < 17 km in the vertical and > 1000 km in the horizontal are less than 50% sensitive, see Figure 2c of Hindley et al. (2019). GWs with short horizontal and long vertical wavelengths carry the majority of GW momentum flux, making AIRS observations suitable for characterising MF (Wright et al., 2021). The noise of this retrieval was quantified by Hindley et al. (2019) and is $\sim$1.5 K for the southern hemisphere winter. The study region is presented in Figure 1 with labels for the key regions we discuss in this paper.

2.2 ERA5 reanalysis

We use data from the ERA5 reanalysis (Hersbach et al., 2020) to provide large scale winds for context and background fields for ray-tracing. ERA5 is a widely-used reanalysis product provided by the European Centre for Medium-Range Weather Forecasting (ECMWF). For the ray-tracing we require inputs of the background atmospheric state and the wave properties. We use zonal and meridional wind, surface pressure, geopotential and temperature at three-hourly time resolution. We remove small-scale perturbations using the separation of scales method i.e. by applying a spectral cutoff at zonal wavenumber 18 described by Strube et al. (2021) and smooth in the meridional and vertical directions. We then interpolate this background onto a $1^\circ \times 1^\circ$ latitude-longitude grid, with a 0.5 km vertical resolution between 2-39 km altitude. Due to the high topography of the Southern Andes and parts of Antarctica we do not trace rays below 2 km altitude, and consider this to represent ground level.

3 Method

3.1 Deriving gravity wave properties from AIRS data

We remove the large-scale dynamics from AIRS observations by subtracting a fourth-order polynomial in the cross-track direction at each height (e.g. Wu, 2004; Alexander & Barnet, 2007; Hoffmann et al., 2016; Wright et al., 2017; Hindley et al., 2019). We next re-grid the data onto a regular distance grid and perform spectral analysis to derive GW properties.

We use a three dimensional spectral analysis method known as the 2D+1 S-transform (ST) method and described by Wright et al. (2021). This method uses a 2D-ST in the horizontal in combination with vertical phase shift estimation to compute horizontal and vertical wavelengths and corresponding amplitudes. Unlike a Fourier transform, the ST lets us spatially locate GW frequency peaks, and is commonly used in GW analysis (e.g. Fritts et al., 1998; Alexander et al., 2008; McDonald, 2012; Wright & Gille, 2013). The 2D+1 method builds upon the 1D method originally applied to AIRS data by (Alexander & Barnet, 2007), the subsequent 2D method developed by Hindley et al. (2016), and is a refinement of the 3-D method described in (Hindley et al., 2019) and first applied in Wright et al. (2017). Once we obtain the spectral properties, we identify GWs in the data by locating regions of consistent horizontal wavelength. This relies on the premise that GWs have approximately consistent horizontal wavelengths across their extent, whilst background noise leads to random wavelength measurements for each pixel with no relation to their neighbours. The method produces a binary mask identifying whether or not a wave is present for each pixel of AIRS data.

We use the 39 km altitude data level, which lies at the centre of AIRS's useful retrieval height range and thus provides the most reliable determination of GWs' vertical wavelengths by avoiding truncation effects. This level also exhibits low noise relative to other heights (Hindley et al., 2019).

Finally, following Ern et al. (2004), we calculate absolute vertical flux of horizontal pseudo-MF (hereafter simply 'absolute MF') at the observation height as,

$$|\mathrm{MF}| = \sqrt{\mathrm{MF_x}^2 + \mathrm{MF_y},^2}$$

$$\left(\mathrm{MF_x}, \mathrm{MF_y}\right) = \frac{\rho}{2m}\left[\frac{g}{N}\right]^2\left[\frac{T'}{\bar{T}}\right]^2\left(k, l\right),$$

where $\mathrm{MF_x}$ and $\mathrm{MF_y}$ are the zonal and meridional MF respectively. k and l represent the horizontal wavenumbers in the zonal and meridional directions, and m in the vertical; g is acceleration due to gravity, N is the Brunt Väisälä frequency, which we assume to be $0.02\,\mathrm{s^{-1}}$, and T' and $\bar{T}$ are the wave amplitude and background temperature respectively. ρ is the atmospheric density.

3.2 Backwards ray-tracing

We use the Gravity wave Regional Or Global RAy Tracer (GROGRAT), originally introduced in Marks and Eckermann (1995). GROGRAT is based on the GW dispersion relation and wave tracing equations of Lighthill (1967), which describe position and wavenumber along the ray path as,

$$\frac{d\mathbf{x}}{dt} = \frac{\partial\omega}{\partial\mathbf{k}}, \frac{d\mathbf{k}}{dt} = -\frac{\partial\omega}{\partial\mathbf{x}}.$$

Where $\mathbf{x}$ and $\mathbf{k}$ are vectors denoting the wave's spherical position and wavenumbers respectively, and ω is the wave's ground-based frequency. We use a modified version of GROGRAT which incorporates the great-circle correction described by Hasha et al. (2008).

GROGRAT was initially designed to trace waves forward in time, i.e. to determine wave propagation from a specified source and properties. A later update to GROGRAT (Eckermann & Marks, 1997) allowed for backwards ray-tracing of waves, and we use this approach.

Each pixel of AIRS data that is identified as a wave is used to initialise a separate ray. We calculate the intrinsic frequency ($\hat{\omega}^2$) as

$$\hat{\omega}^2 = \frac{\mathrm{N}^2\left(k^2+l^2\right)+f^2\left(m^2+\frac{1}{4H^2}\right)}{k^2+l^2+m^2+\frac{1}{4H^2}} \tag{1}$$

and use the ERA5 background winds to convert this to ground-based frequency (ω^2),

$$\omega^2 = \hat{\omega}^2 + ku + lv. \tag{2}$$

Finally, we calculate the wind wave amplitude, $\hat{u}$, from the AIRS observed temperature amplitude using the polarisation relation,

$$\hat{u} = \frac{g}{N}\frac{T'}{\bar{T}}\left[1-\left(f/\omega\right)^2\right]^{-1/2} \tag{3}$$

Where N is the Brunt-Väisälä frequency. k, l and m are wavenumbers in the zonal, meridional and vertical. $f = 2\Omega\sin\phi$ is the Coriolis parameter at latitude ϕ and H is the scale height. u and v are the ERA5 background zonal and meridional winds.

We output the ray location (i.e. latitude and longitude) at 1 km altitude increments, tracing the ray downwards from 39 km until the ray terminates. Typically, GROGRAT terminates rays because (i) the ray has reached the bottom of the prescribed atmosphere, (ii) the ray has reached a critical level and stalls vertically (i.e. has a vertical velocity $<0.01\,\mathrm{ms^{-1}}$) and a small minority of rays terminate due to (iii) vertical reflection which is not supported by GROGRAT. This means that waves will sometimes terminate at their source, but can also be traced backwards through the source without terminating. Unfortunately, this means that rays can travel to the ground whilst the real source of the wave could lie somewhere along the ray path (Preusse et al., 2014). In our results, we find that 61% of all rays terminate because they have reached the ground; this percentage will be a combination of correctly traced orographic waves as well as rays that have been back-traced through non-orographic sources and continued downwards to the ground. The height at which the ray terminates is referred to as the lowest traceable altitude (LTA). Finally, it is important to note that this method is not perfect. Rays may be mis-traced, meaning that the path the ray takes deviates from the real path of the GW. This can happen for several reasons, including instrument noise/errors in the observation of GWs, method errors in determining GW properties, or inaccuracy of ERA5 background wind fields.

Figure 2 demonstrates our method as applied to an example swath of AIRS data, recorded on the 4th June 2010 at ∼04:00 UTC. Panel (a) shows temperature perturbations at 39 km altitude, and panel (b) shows the areas identified by our masking technique as GWs. Panel (c) shows the rays we trace backwards from this wave; the rays are shown as green lines, and one has been initialised from each pixel of AIRS data at 39 km.

In this example, most rays terminate because they reach the bottom of the specified background (2 km altitude): one group of rays travels almost directly downwards towards the Antarctic Peninsula (approximately 65°W, 65°S), whilst another traces back to the Southern Andes, possibly due to refraction in the jet (Dunkerton, 1984; Sato et al., 2011; Wright et al., 2017). The ray path towards large mountain ranges and all the way down to 2 km suggests that the orography is the likely source of these GWs.

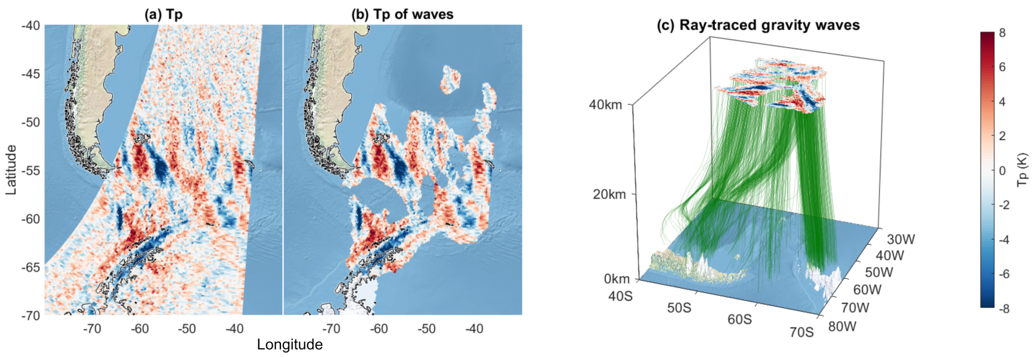

Figure 2. An example of a ray-traced overpass from AIRS from 4th June 2010 at approximately 04:00 UTC. Panel (a) shows the temperature perturbations at 39 km from AIRS. Panel (b) shows the temperature perturbations of pixels that are identified as GWs. Panel (c) shows the ray-tracing. The original masked GWs are shown at the top with rays coloured in green descending back towards the Southern Andes and Antarctic Peninsula mountain ranges. Each pixel of AIRS data is used to initialise a ray at 39 km.

3.3 Post processing of traced rays

Backwards ray-tracing five months of detected waves from all AIRS data from May - September 2012 results in 14.2 million rays which we then analyse in a number of different ways. We first investigate the meridional propagation of GWs by considering the difference between their observed latitude (i.e. the latitude at which they are observed by AIRS at 39 km altitude and where a ray is initialised) and the latitude the ray is then traced back to lower in the atmosphere. This provides an estimate of the meridional propagation distance of the waves to where they are observed in the stratosphere by AIRS.

Secondly, we investigate the propagation of GWs from specific orographic sources: the Southern Andes, Antarctic Peninsula, Prince Charles Mountains, Transantarctic Mountains, South Georgia and Kerguelen (Figure 1). To do this, we consider all the rays that are traced back to chosen regions with a lowest traceable altitude of <5 km and explore how far away these waves are observed in the stratosphere by AIRS.

Thirdly, we divide waves that are traced to land and ocean and present the observation location and respective momentum fluxes from these two classes. This quantifies the proportion of momentum flux traced to land and ocean, providing an estimate of the split between orographic and non-orographic GW activity to the observed stratospheric momentum flux in this region. This is an upper estimate of orographic activity as sources over land may also be non-orographic. We note that due to AIRS' polar orbit, we have more observations and hence initialise more rays at high latitudes. To compensate for this effect, in this work we consider daily mean results of MF as almost the whole area poleward of 30°S is observed by AIRS at least once per day.

Finally, we further divide the geographical regions (including small islands) and quantify GWs traced back to different areas and weighted by their daily mean observed stratospheric momentum flux. This quantifies the proportion of observed MF in the stratosphere that is traced back to each region. A key point here is that we do not claim this represents all MF originating from each region: we explicitly only trace rays that are observed by AIRS in the stratosphere, and hence these waves must have been able to propagate up to these altitudes without dissipating or being critical level filtered and in addition must be observable to AIRS.

4 Results

4.1 AIRS observations and background winds

Figure 3 shows AIRS observations of GWs and ERA5 zonal winds at 39 km altitude. The left column shows the total number of GWs observed each month. In the middle column, we scale these totals by the number of AIRS overpasses to give an occurrence frequency. We note that all regions in our study area are observed by AIRS at least once every 12 hours.

Both GW metrics show localised hotspots, as well as general activity over the ocean and Antarctic continent extending northwards to ∼20°S. Overall, GW activity increases from May until mid-winter (July and August) before tailing off. This seasonal peak agrees with and is likely to be related to the background wind structure, which also peaks in strength in mid-winter. It is well-known that the Southern Andes act as the largest individual source of GW activity in this region and arguably the whole Earth system, as first identified by (Eckermann & Preusse, 1999), confirmed with AIRS (Hoffmann et al., 2013; Hindley et al., 2020), GPS-RO (Hindley et al., 2015), the SABER, MLS and HIRDLS limb sounders (Alexander et al., 2008; Wright & Gille, 2013; Geller et al., 2013; Wright et al., 2016; Ern et al., 2018; Wu & Eckermann, 2008), and the Aeolus Doppler wind profiler (Banyard et al., 2021). Other orographic GW hotspots of GWs can also be seen in our data, including the Antarctic Peninsula, South Georgia, Kerguelen, the Prince Charles Mountains, the Transantarctic mountains, Tasmania and New Zealand. We see 'tails' of GW activity downstream of orographic sources, particularly from the Southern Andes and Antarctic Peninsula extending into the Drake Passage. We also see GW activity over the open ocean away from clear orographic sources. The exact sources of these GWs remain unclear and difficult to attribute. Finally, the observed GW activity clearly shares key morphological features with the zonal wind field at the same height, presented in the right column. The polar night jet sits above the Southern Ocean during all five months, maximising in strength at ∼80 ms^{-1} in July. Observed GW activity follows the jet centre, and a stronger jet correlates spatially and temporally with stronger GW activity. This is due to (1) refraction to longer vertical wavelengths which increases visibility to AIRS and (2) actual geophysical lateral propagation of GWs into the center of the jet, which has been shown in observations e.g. (Hindley et al., 2015; Wright et al., 2017; Hindley et al., 2020) and is discussed in the next section below.

4.2 Convergence of gravity waves to 60°S

Numerous studies have hypothesised that a significant proportion of the "missing" MF at 60°S in chemistry-climate models reaches 60°S via meridional convergence (McLandress et al., 2012; Strube et al., 2021; Moffat-Griffin et al., 2020; Hindley et al., 2015; Wright et al., 2017; Geller et al., 2013, and others). In particular, persuasive evidence has been shown of orographic waves from the Southern Andes and Antarctic Peninsula converging in this way: in a numerical modelling study, Sato et al. (2011) used the high vertical resolution Kanto model (Watanabe et al., 2008) to show that rays launched from the surface of the Andes and Peninsula would be expected to exhibit this convergence, while observationally, Hindley et al. (2015) demonstrated that GW potential energies derived from Global Positioning System Radio Occultation (GPS-RO) measurements showed evidence of this convergence southwards from the Southern Andes, but did not find evidence for northward propagation from the Peninsula using 2010 data. Wright et al. (2017), meanwhile, used instantaneous AIRS-observed group speeds over the Drake passage to infer convergence from both the Andes and the Peninsular based on observed wave orientation. They found that the orientation of the waves turn in the wind, demonstrating that the refraction of the waves in the background winds plays a role in their lateral propagation.

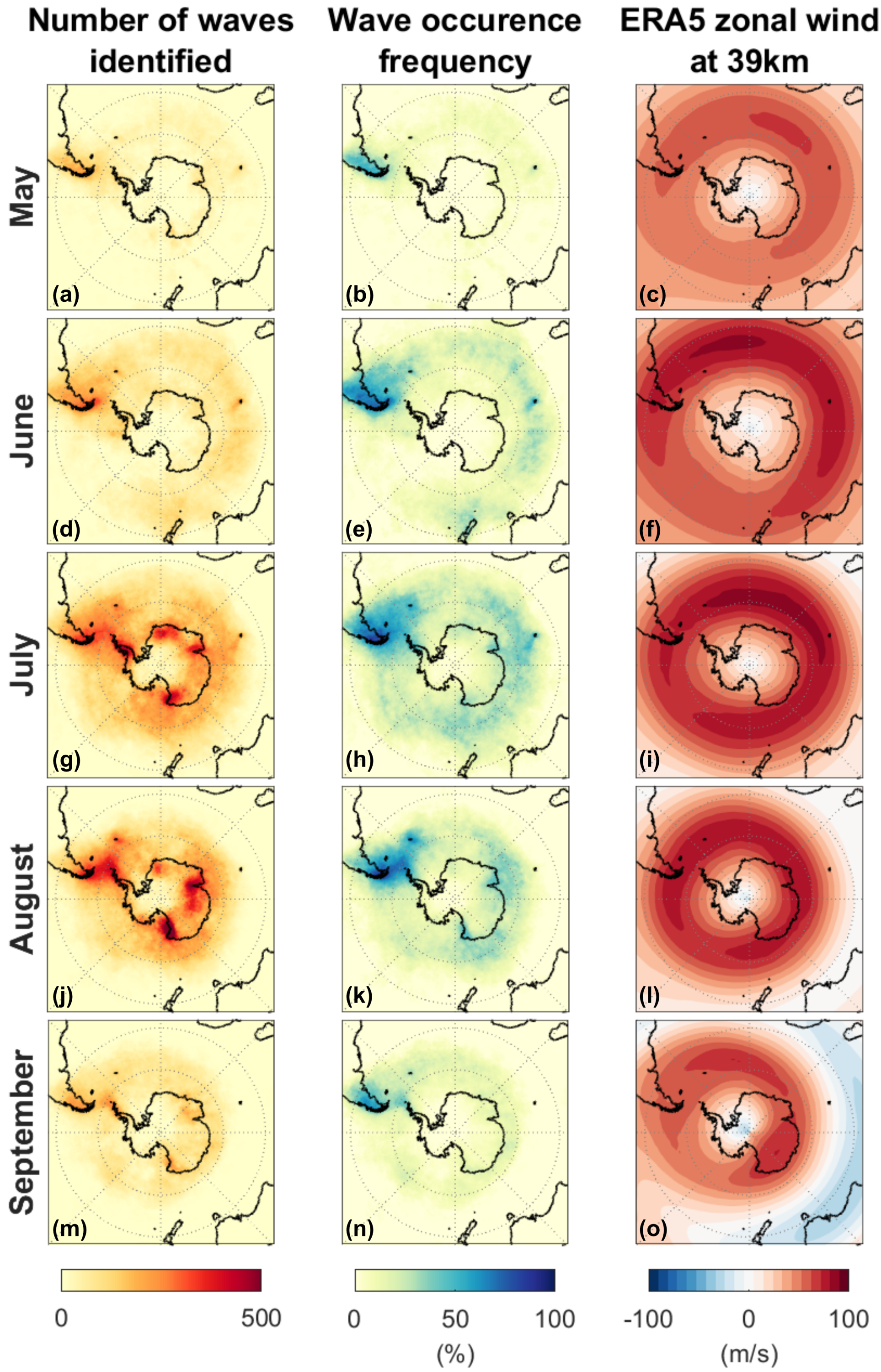

Figure 3. AIRS observed GWs and ERA5 background winds. Left column, the total number of GW observations at 39 km altitude from AIRS. Middle column, GW occurrence frequency at 39 km from AIRS calculated from number of waves identified per overpass. Right column, ERA5 zonal winds at 39 km.

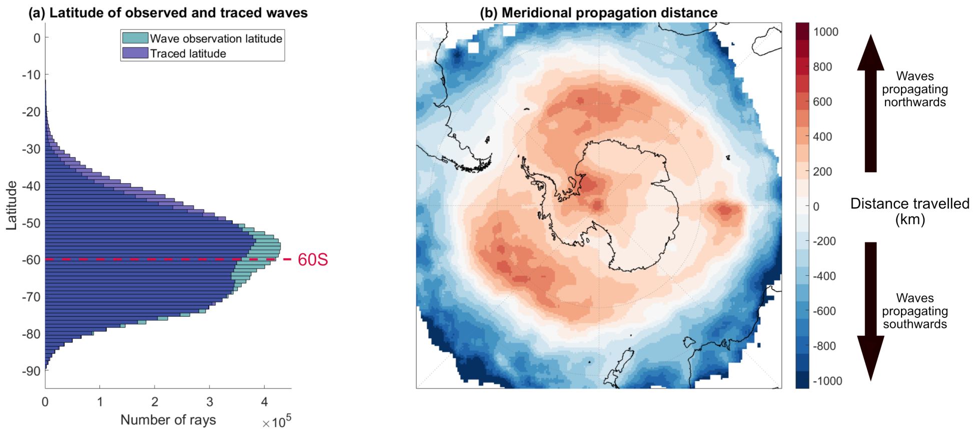

Figure 4. Meridional propagation of rays. Panel (a) shows a histogram of the observation and traced latitude of the waves. We define the GW "observation" latitude as the latitude that AIRS observes at the GW at 39 km, and the "traced" altitude as the lower-altitude latitude which the ray traces back to. (b) shows the average meridional distance travelled by the rays in km positioned by the traced position of the ray (i.e. the source location of the GW).

Ray-tracing allows us to investigate this. To do so, we first compare the start and end locations of our 14.2 million rays as a function of latitude. Figure 4a shows the results of this analysis as a pair of overlaid histograms. For clarity of discussion, we define the GW "observation" latitude as the latitude that AIRS observes at the GW at 39 km, and the "traced" altitude as the lower-altitude latitude which the ray traces back to. The observation-level distribution of waves, shown in cyan, forms a near-Gaussian distribution centred around 55°S, consistent with Figure 3. The traced latitude (dark blue), however, produces a bimodal distribution, with a local minimum at ~60-65°S. This suggests that the GWs seen by AIRS around 60°S are largely generated by sources significantly north and south of where they are observed in the stratosphere. The peak centred at 55°S is larger than the peak centred at 70°S, suggesting that sources to the north play a slightly larger role in the observational-level peak near 60°S.

Figure 4b characterises how far these rays propagate meridionally. Specifically, we show the difference between the observation latitude and the traced latitude. Positive values (red) indicate that on average waves have propagated northwards from their source to the observation altitude, while negative (blue) values indicate that waves have propagated southwards. We see northwards propagation over the Antarctic continent and near-continental regions of the Southern Ocean and southward propagation from more equatorward regions of our map. We find local minimum over and near orographic sources of gravity waves (the Southern Andes, the Antarctic Peninsula, South Georgia, Kergulen and New Zealand) this is likely due to the high frequency of wave events. Equally, regions which show a local maximum of lateral propagation are typically have lower gravity wave activity.

Over Antarctica, waves generally propagate ~200-600 km northwards, travelling outwards over the Southern Ocean into the jet core. Over the ocean itself, meanwhile, meridional wave propagation averages out between north and south; this is because of the shifting jet-centre location, and hence represents a shifting focus. Further north, our results suggest that waves can propagate meridional distances as large as 1000 km from source to observation; however, in practice the number of waves seen here is small and hence inaccurate traces may contribute significantly to this mean.

This result is the first time convergence to 60°S has been demonstrated across all longitudes of the Southern Ocean by backwards ray-tracing observations, providing a vital quantitative constraint on the average distance travelled by these waves. This suggests that all GWs, both orographic and non-orographic, converge towards 60°S and hence that both may contribute significantly to the missing MF at 60°S. The significance of this result is that it expands on previous conclusions of the modelling study of McLandress et al. (2012), who focused on orographic waves but concluded that a significant non-orographic contribution was unlikely. It does however, agree with the observational work of Hindley et al. (2016) and Holt et al. (2017), who used AIRS observations and found that directional MF (in Hindley et al., 2016) and wave propagation direction (in Holt et al., 2017) visible to AIRS converged towards 60°S at all longitudes.

Our results apply only to GWs in the observational filter range of AIRS. However, we can make inferences about other parts of the observational filter from work using other datasets. Specifically, Moffat-Griffin et al. (2020) carried out a comprehensive study of GWs observed by radiosondes launched from 11 different sites in Antarctica, the Southern Andes and from small islands in the Southern Ocean. They calculated the angular distribution of momentum flux for 12-30 km altitude and found that for sites poleward of 60°S, the momentum flux was northwards and for sites at lower latitudes, the momentum flux was southwards. This again suggests a convergence of gravity waves towards 60°S. The observational filter of radiosondes and AIRS observations do not overlap (Alexander et al., 2010; Wright et al., 2016), yet we also see suggested convergence to 60°S all around the Southern Ocean, not just over the Drake Passage. This suggests that our results may generalise across the GW spectrum. This radiosonde dataset may also cover some of the same waves we trace from AIRS at 39 km however at lower wind velocities at lower altitudes.

4.3 Lateral propagation of orographic gravity waves

We next explore the horizontal propagation of GWs from orographic sources. We do this by considering all rays that trace back to defined regions over orography and which terminate at altitudes less than 5 km. This is shown in Figures 5-7; here, colours show the number of rays traced back to each region, with the ERA5 westwards wind at 39 km shown in greyscale. Figure 5 shows the Southern Andes (blue), Figure 6 shows the Antarctic Peninsula (blue), the Prince Charles Mountains (red) and the Transantarctic Mountains (green), and Figure 7 shows South Georgia (blue), Kerguelen (green) and New Zealand (red). These regions were selected from the hotspots found in Figure 3.

In Figures 5-7, we see that the overwhelming majority of waves are observed directly above the region that they trace back to. This suggests that the majority of the AIRS-observed waves travel almost directly upwards. AIRS is particularly sensitive to long-vertical-wavelength waves, which tend to have fast vertical phase speeds and thus are expected to behave in this way. Despite this, in all cases we see trails of waves propagating downstream from each orographic region. This is particularly clear for the Southern Andes (Figure 5), where GWs observed hundreds of kilometres downstream can be traced back to < 5 km altitude here. This is consistent with Sato et al. (2011), their Figure 5, who launched waves from the Southern Andes and Antarctic Peninsula with horizontal wavelengths of 300 km and a ground-based phase speed of zero through idealised background conditions. These rays propagated laterally up to 50° eastwards before reaching 40 km in altitude. The SOUTHTRAC-GW campaign which comprehensively explored GW dynamics over the Andes (Rapp et al., 2021) with airborne observations and high resolution modelling found compelling evidence of refraction of gravity waves into the polar night jey and subsequent eastwards propagation towards 60°S. Recently, Krasauskas

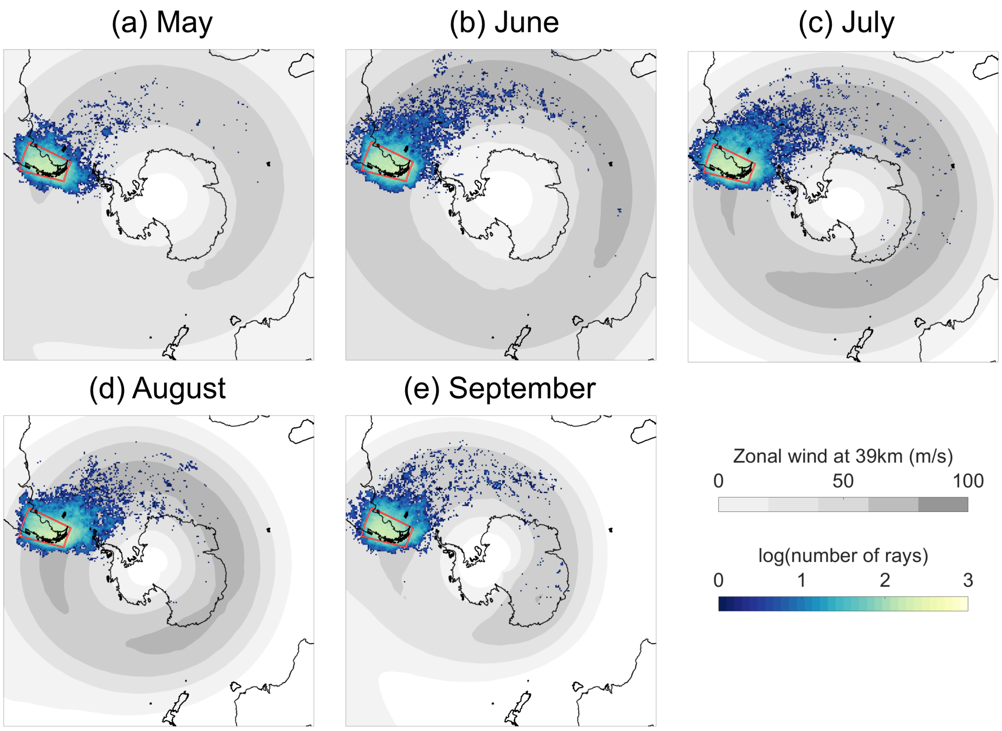

Figure 5. The observation location of all rays traced back to the Southern Andes. Color denotes the number of rays traced back to the red box (log10 scale). Grey contours show the ERA5 westward winds at 39km.

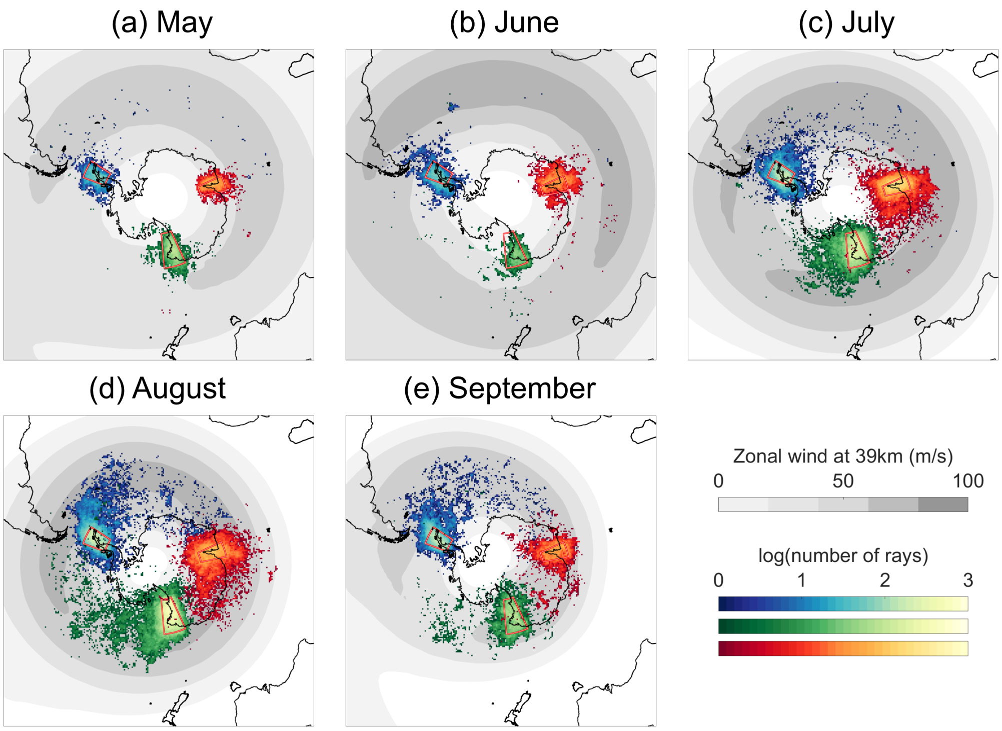

Figure 6. The observation locations of all rays traced back to key orographic source regions on the Antarctic Continent. Colour denotes the number of rays traced back to each red box (log10 scale). The Antarctic Peninsula (blue), Transantarctic Mountains (green) and the Prince Charles Mountains (red). Grey contours show the ERA5 westward winds at 39km.

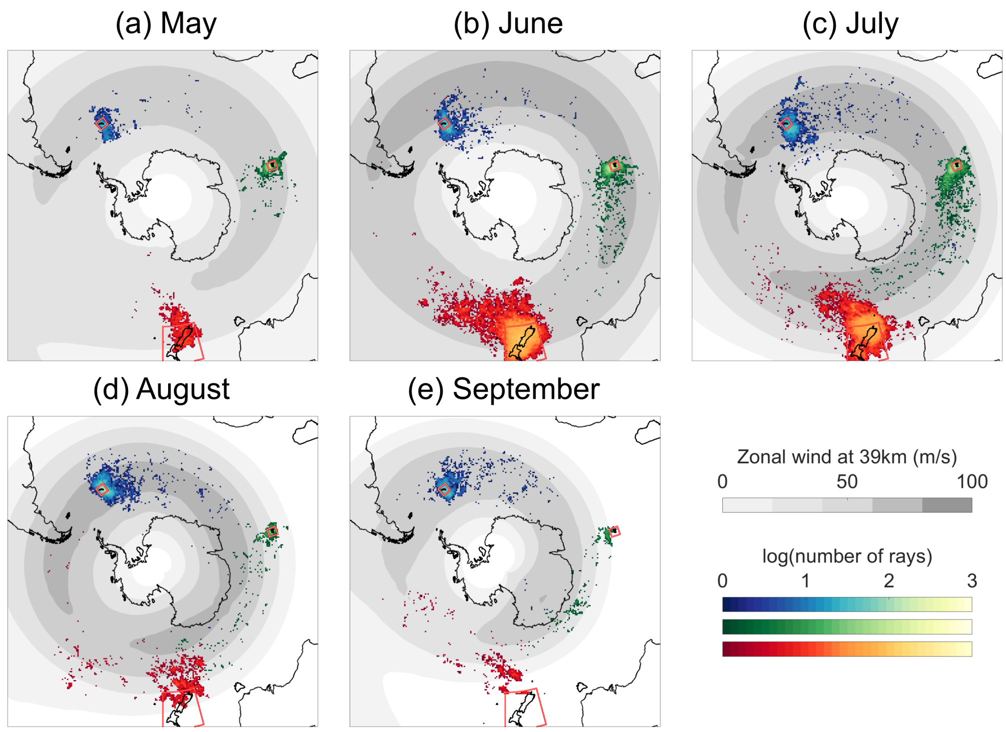

Figure 7. The observation locations of all rays traced back to key island source regions. Colour denotes the number of rays traced back to each red box (log10 scale). South Georgia (blue), Kergulen (green) and New Zealand (red). Grey contours show the ERA5 westward winds at 39km.

et al. (2023) investigated the oblique propagation of gravity waves over the Southern Andes in a multi-instrument case study using GLORIA measurements at 8-15 km altitude and observations from the Airborne Lidar for Middle Atmosphere research (ALIMA) at 20-80 km in height. In a case study in September 2019, they used forwards ray tracing from GLORIA inputs and compared traced ray properties to ALIMA observations. This allowed them to directly observe horizontal refraction of orographic gravity waves in the strong stratospheric winds for the first time.

Recently, Rhode et al. (2023) devised a mountain wave model for quantifying the horizontal propagation of orographic gravity waves. This model is based on identifying ridges from topography data, determining gravity wave launch parameters then forwards tracing waves from the mountains to predict MF at higher altitudes. Comparison with HIRDLS satellite data showed promising agreement, validating their model. Their predicted gravity wave activity, in particular the downstream propagation patterns agree well with the findings of our study, 'tails' of gravity wave activity are found downstream of the Southern Andes, Antarctic Peninsula, Kerguelen, Tasmania and New Zealand of similar shape which also peak throughout June and July. This mountain wave model was implemented in a parametrisation which redistributes GW MF horizontally by Eichinger et al. (2023) and they found a reduction in model biases as a result. This agreement between the mountain wave model (Rhode et al., 2023) and our findings here, as well as an improvement in model biases (Eichinger et al., 2023) shows a promising pathway to improving GW parametrisations.

Throughout all months, in agreement with Figure 4, we also see orographic waves converging towards 60°S. It is especially clear in August, where waves from the Andes propagate south-east (Figure 5d) and waves from the Peninsula north-east (Figure 6d) between surface and the stratosphere. In this month, we also see waves traced back to Kergulen from south-east of the island (Figure 7d), i.e. propagating into the jet.

The propagation pathways of our traced GWs vary significantly by region and by month, which we attribute primarily to stratospheric background wind variability. The strong jet biases our observations of stratospheric GWs in two ways: (1) the strong westerly winds preferentially allow westward propagating GWs to propagate to observation levels (Hindley et al., 2016) and (2) GWs are refracted to longer vertical wavelengths in the strong winds, making these waves more observable by AIRS (Hindley et al., 2019). The first of these effects acts as a real control on the MF present in the system, however, the second acts on our results as an observational bias. The variation of GW activity with the background wind is consistent with the results of Hoffmann et al. (2016), who correlated AIRS-observed orographic GWs separately with (a) surface winds and (b) stratospheric winds, and found that observation-level winds exhibited a much higher correlation with GW activity, which they attributed to observational filter effects.

We also see that regions of stronger wind correlate with longer "tails" of rays downstream of orographic sources. This is particularly clear over Kerguelen: the GW "tail" here is most prominent in July (Figure 7c), when the jet allows for GW propagation and also refracts them to longer wavelengths. GWs originating over New Zealand also exhibit this effect in May (to some extent), June and July (Figure 7b,c), when the jet reaches further north. The activity of the polar night jet provides a plausible mechanism for the high level of GW intermittency seen over Kerguelen and New Zealand in studies such as Wright et al. (2013).

Waves traced back to South Georgia exhibit a ship wave pattern (Eckermann et al., 2016) with two downstream tails, one to the north-west and another to the south-west. This is because South Georgia lies almost in the centre of the jet, allowing waves to propagate upwards. This was seen previously by Hindley et al. (2021) in snapshots of GW observations by AIRS. Kerguelen is another isolated island and also produces this pattern when the background wind conditions allow it (Figure 7c, for example); however, most of the time, Kerguelen lies north of the jet, and hence we do not observe the ship wave pattern here.

GWs over the Prince Charles mountains and Transantarctic mountains are thought to be generated by strong katabatic winds flowing off the continent (Watanabe et al., 2006). Whilst this source has not been extensively studied previously, such katabatic surface winds propagate northwards and hence should result in GWs with phase fronts aligned parallel to the stratospheric jet. Waves generated over the Southern Andes and Antarctic peninsula, however, have phase fronts perpendicular to the winds of the jet. This difference may explain why GWs from the Prince Charles mountains and Transantarctic mountains do not propagate as far downstream.

4.4 Orographic and non-orographic sources of gravity waves

We next use our traced rays to separate the observed GWs into those that are traced back to land (defined as land areas plus an extra 200 km coastline) and those that trace to the ocean. Figure 8 shows the mean number of rays traced to land (left column), sea (middle column) and total for each month. Figure 9 presents the same division of rays weighted by the observed stratospheric MF of each ray. We calculate the monthly average from daily mean values to correct for the polar orbit of AIRS (as all regions presented are observed at least once every 24 hours). What is perhaps most striking in these plots is the tails of GW activity found downstream of small islands, in both the number of rays (Figure 8) and momentum flux (Figure 9). In particular, downstream of Kerguelen and Heard island (a small island to the south-west of Kerguelen, 53°S 73°E) in August we see a large downstream tail of rays with significant momentum flux that traces back to land (Figures 8j and 9j) and consistent with the results presented in Figures 5 to 7.

We previously discussed the propagation and behaviour of orographic GWs in Figures 5 - 7, so here we focus our discussion on the waves that do not trace back to land (middle column of Figures 8 and 9). These exhibit some interesting results. Firstly, there is a surprising peak of GW activity in the Drake passage between the Southern Andes and the Antarctic Peninsula. This feature is present throughout all months but is perhaps most evident in mid-winter (Figures 8 and 9 panels e,h,k). This suggests that a significant number of waves are observed in the Drake Passage and not traced back to orography. Considering the number of rays (Figure 8 panels e,h,k), we see that the Drake Passage is dominated by a high number of wave observations that are traced back to the sea. However, in the associated absolute MF of this region (Figure 9 panels e,h,k), we see a pattern of higher MF only to the south-east of the tip of the South America and downstream from there, suggesting that the shape of the land plays a role. We have three possibly hypothesises for the increased wave activity in the Drake Passage which may all contribute to some extent. (1) high MF orographic GWs from the Southern Andes and Antarctic Peninsula which have propagated downstream and converge around 60°S that are mis-traced by the backwards tracing. (2) lower MF waves generated upstream of the Southern Andes possibly by storms funnelling into the Drake Passage or (3) gravity waves generated by an orographic-jet mechanism. Geldenhuys et al. (2021) presented the first observational evidence of such orographic-jet generation using GLORIA observations from a campaign over Greenland. They describe how orography modifies the wind flow over large scales resulting in an 'out of balance jet' which then excites gravity waves. There are also small hotspots of MF downstream of Kerguelen and South Georgia visible in the absolute MF of waves, which are traced back to the sea (June and July, Figure 9-middle panels), suggesting that hypothesises (1) and (3) may also influence other regions downstream of orography.

Another striking feature of the waves traced back to sea is the hotspot of activity over the ocean stretching from the south of Africa ($\approx 30°$W) clockwise around the con-

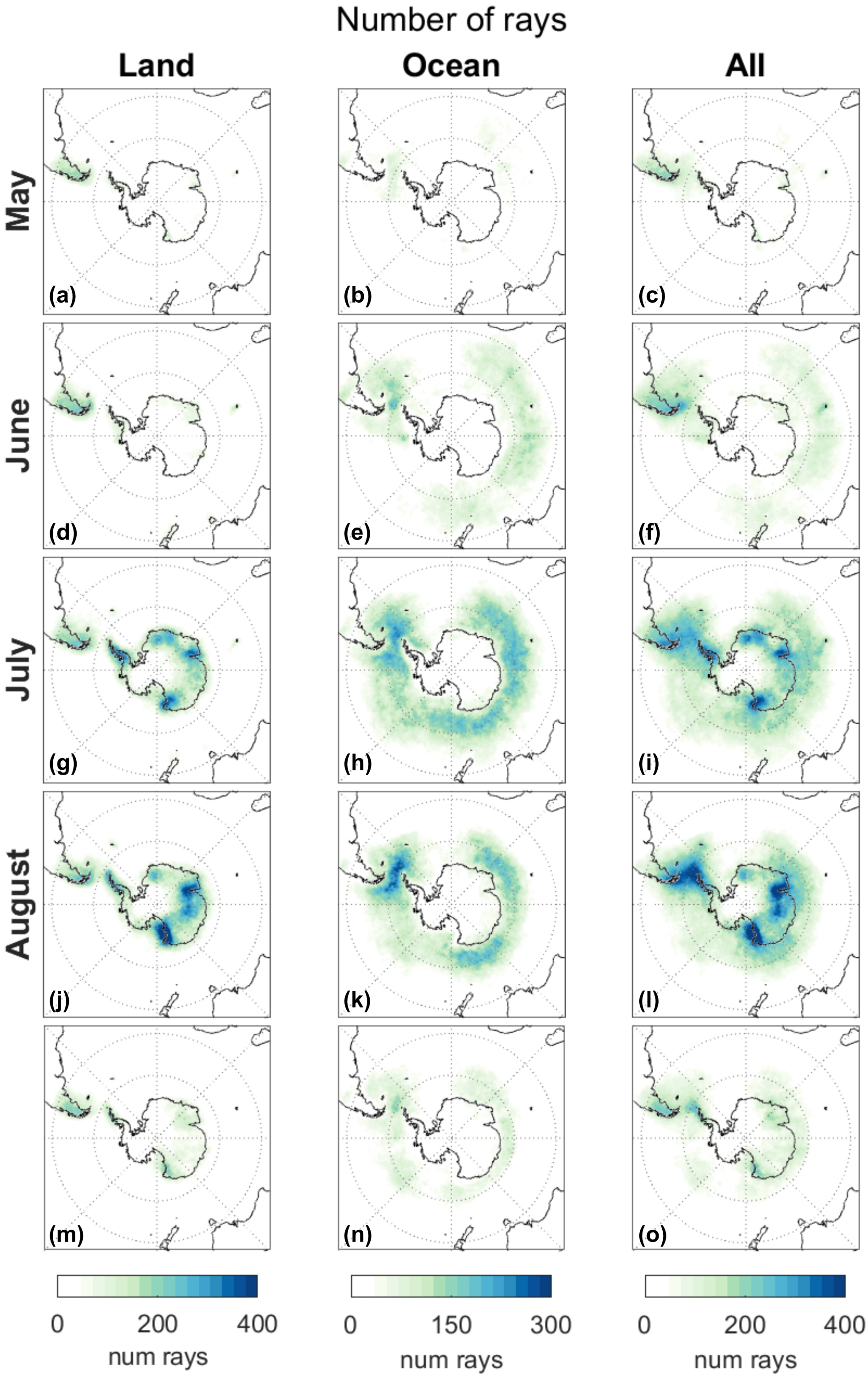

Figure 8. Number of rays traced back to land (left column), ocean (middle column) and both (right column), positioned by the observation location of the ray.

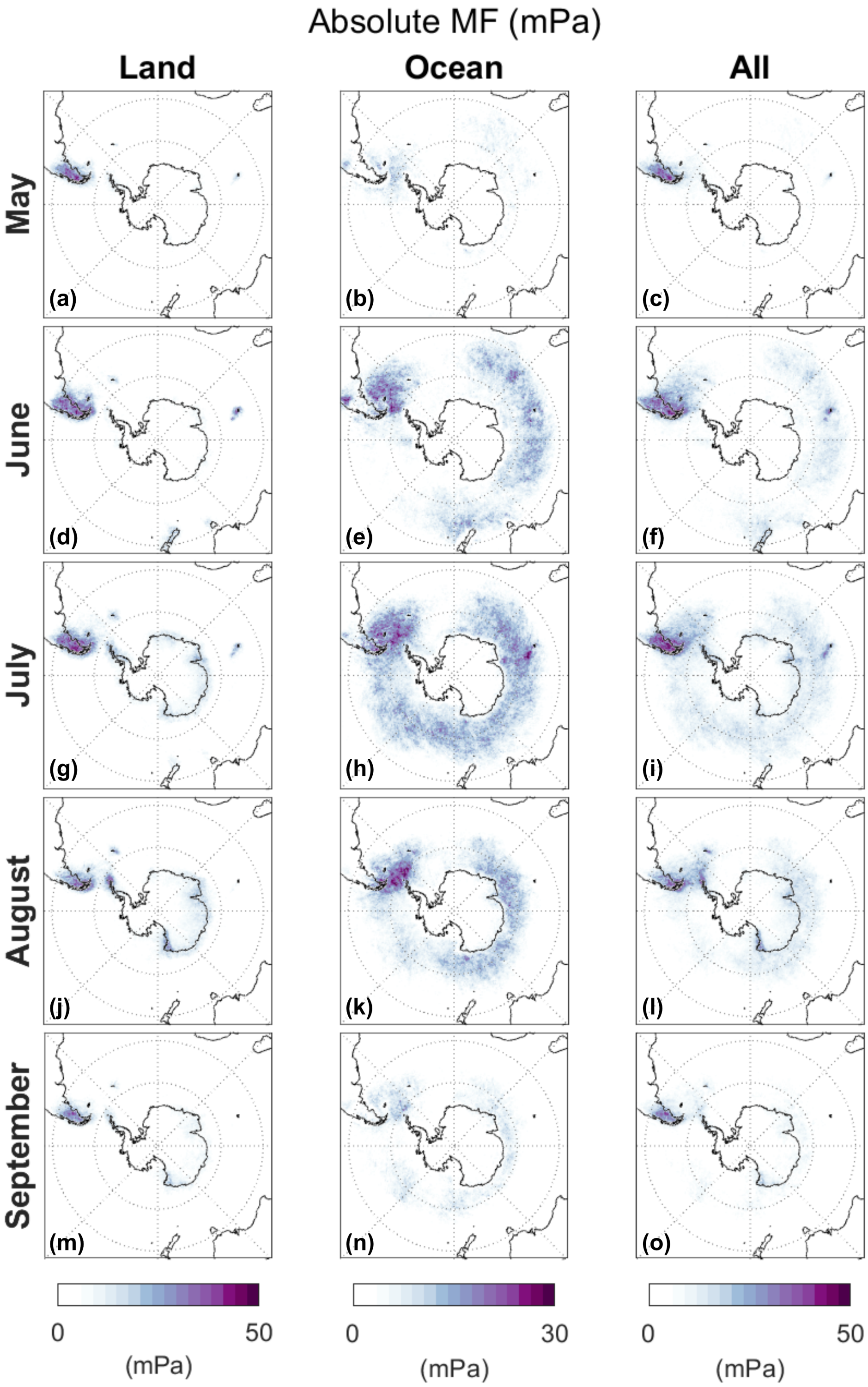

Figure 9. Absolute Momentum Flux (mPa) of rays traced back to land (left column), ocean (middle column) and both (right column), positioned by the observation location of the ray.

tinent. There is a clear gap between activity upstream of here. Non-orographic sources have not been explored in detail in previous studies; however, Hendricks et al. (2014) suggests that some of these hotspots may be attributable to storms. Holt et al. (2017) investigated absolute MF from a high-resolution GEOS5 Nature Run in relation to both precipitation and frontogenesis. They found that fronts and precipitation were weakly correlated with absolute MF between 30°S-80°S at most longitudes, although correlations were higher at the lower latitudes. Plougonven et al. (2017) explored the relationship between wind speeds and GWs in the lower stratosphere in a mesoscale model (which would not suffer from the observational filter problem that observations do) and found that large values of non-orographic MF was more likely in regions of strong winds. They suggest several possible reasons for this, including spatial variations in tropospheric sources, lateral propagation, local generation of GWs in the stratospheric winds or vertical wind shear. More recently, Green et al. (2024) calculated momentum fluxes from Project Loon superpressure balloon data. They analysed the relationship between zonal momentum fluxes in the lower stratosphere (16-21 km altitude) and zonal background winds over the Southern Ocean (excluding orographic regions), and found increasing MF with increasing background winds which they argued are due to a combination of wave sources and filtering.

Strube et al. (2021) used backwards ray-tracing to carry out a case study on propagation paths and sources of gravity waves over New Zealand in the ECMWF-IFS model from 25 km altitude. A strength of this study is in the self-consistency of tracing ECMWF waves through the ECMWF background atmosphere reducing the likelihood of waves being mis-traced. They found that firstly, stratospheric gravity waves are subject to far lateral displacement, in strong agreement with the results of our study (Section 4.2 and 4.3). Secondly, their source attribution revealed that both non-orographic and orographic sources are important in the region around New Zealand and corroborates the findings in our work that non-orographic waves can originate over the open ocean.

In future work using this ray-traced dataset we aim to better quantify the source mechanisms of non-orographic GWs, particularly the puzzling enhancement in the Drake Passage region.

4.5 Momentum flux from different source regions

We next quantify the fraction of observed stratospheric MF which traces back to specific geographic regions, illustrated in Figure 10a. These regions are defined as follows:

- We first split Antarctica into three regions, specifically a Transantarctic region from 0°-135°E, an Antarctic Peninsula region from 135°W-0° and an East Antarctic region from 135°E-135°W
- We next define additional land regions equatorward of Antarctica, specifically (i) the Southern Andes, including the Falkland Islands, (ii) South Georgia, (iii) Kerguelen, including Heard Island, (iv) Australia including Tasmania, and (v) New Zealand.
- Finally, we divide the remaining area into a Drake Passage region (55°-80°W) and a general ocean region covering all remaining areas within 6000 km of the pole.

All defined land regions include a 200 km coastline padding on interfaces with the ocean, as discussed above. Figure 10b shows the proportion of area that each region makes up. The general ocean region covers the vast majority of this region, making up 78% of the area; second largest is the East Antarctic region at 7%, then the Antarctic Peninsula at 5%. At the other end of the scale, small islands such as Kerguelen and South Georgia cover $\sim 0.4\%$ and $\sim 0.2\%$ of the total area.

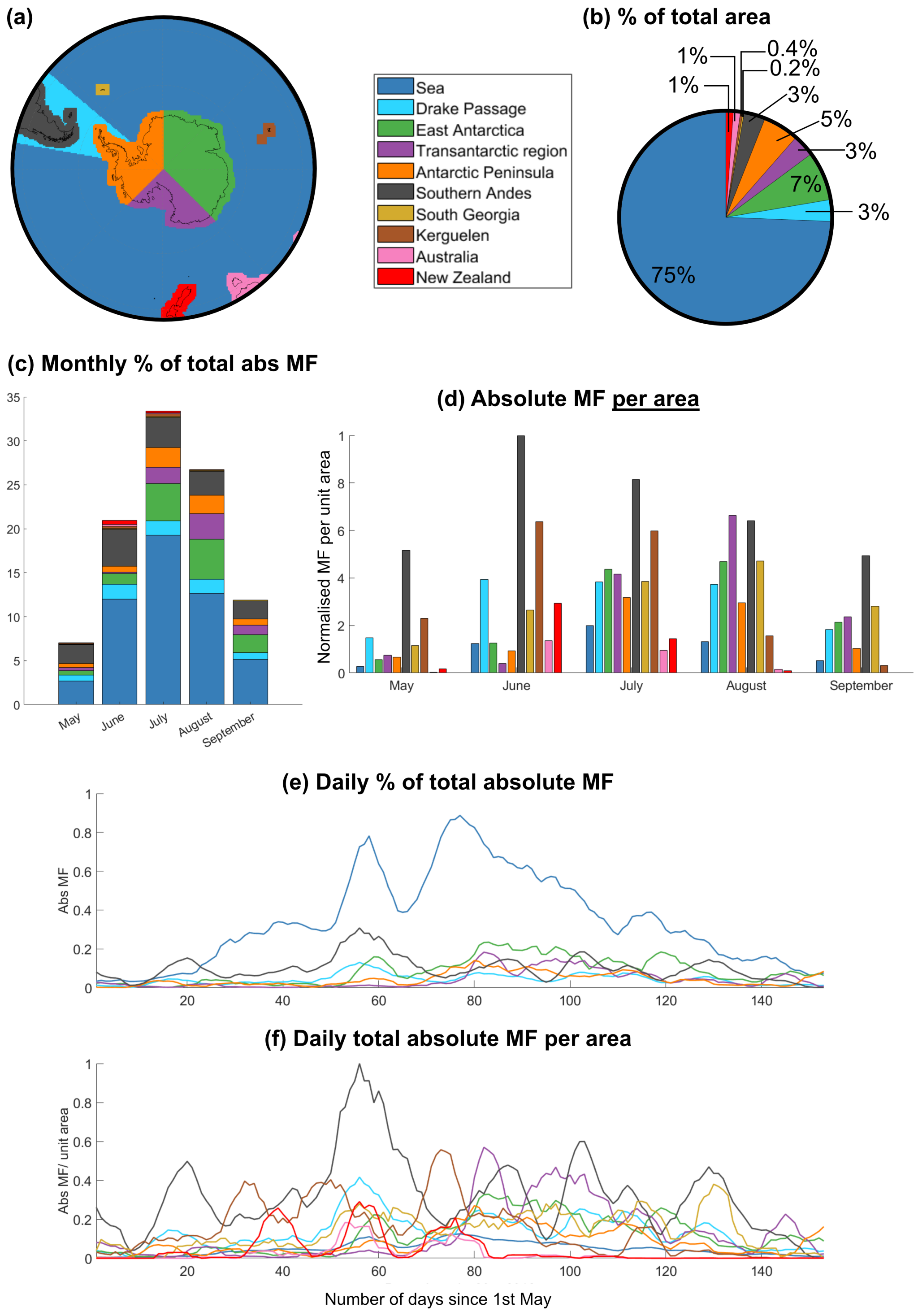

Figure 10. The proportion of observed absolute stratospheric momentum flux traced back to different regions. Panel (a), the different regions. Panel (b) the fraction of the total area that each region makes up, (c) the percentage of total flux split per month and per region, (d) the same absolute momentum flux scaled by the area of each region. Panel (e) shows the daily momentum flux attributed to each region and (f) the daily MF per unit area.

	May	June	July	August	September	Average
Sea	38.6 %	57.3 %	57.8 %	47.3 %	43.1 %	48.8 %
Drake Passage	9.0 %	8.0 %	4.9 %	5.9 %	6.6 %	6.9 %
Total non-orographic	47.6 %	65.4 %	62.6 %	53.3 %	49.6 %	55.7 %
Southern Andes	30.8 %	20.1 %	10.3 %	10.1 %	17.4 %	17.7 %
East Antarctica	7.7 %	5.8 %	12.7 %	17.1 %	17.4 %	12.1 %
Transantarctic region	4.7 %	0.9 %	5.5 %	10.9 %	8.7 %	6.1 %
Antarctic Peninsula	6.7 %	3.2 %	6.7 %	7.8 %	6.1 %	6.1 %
Kerguelen	1.6 %	1.4 %	0.9 %	0.3 %	0.1 %	0.9 %
New Zealand	0.3 %	2.0 %	0.6 %	0.1 %	0.0 %	0.6 %
South Georgia	0.5 %	0.4 %	0.3 %	0.5 %	0.7 %	0.5 %
Australia	0.1 %	0.9 %	0.4 %	0.1 %	0.0 %	0.3 %
Total orographic	52.4 %	34.6 %	37.4 %	46.7 %	50.4 %	44.3 %

Table 1. Percentage of monthly observed stratospheric absolute momentum flux, separated by region traced back to. Columns sum to 100% (when excluding orographic and non-orographic subtotals)

In Figure 10c, we show the percentage of absolute MF attributed to each region. This is computed by considering the location each ray is backwards traced to and weighting this by the observed absolute MF of this ray at its stratospheric start point. For simplicity we scale by the total observed stratospheric MF over May-September (not time-varying values). MF peaks in mid-winter in July, when almost 35% of the overall observed MF across the May-September period is measured.

We clearly see that waves traced to sources over the ocean make up the largest proportion of MF in the stratosphere. The split between orographic and non-orographic sources vary significantly between months: in May, the split between orographic and non-orographic is even, whereas in July momentum flux from non-orographic regions contributes almost two thirds of the total momentum flux observed.

This mix is also illustrated by Figure 10e, where we show the same absolute MF traced to regions (similar to Figure 10c, but as a daily time series smoothed with a 7-day moving mean). We again see that the MF traced to the ocean dominates, and peaks in mid-winter. The second largest-contributing region is the Southern Andes (grey) which shows some temporal variability but is overall more consistent over the time period. In the later winter, i.e. from day 80 onwards, East Antarctica becomes an important source of MF, overtaking the Southern Andes on occasion.

In Figure 10d and 10f, we scale the MF traced back to each region by the area of the region, normalising each time series to a maximum of 1. This thus quantifies the MF originating in each region per unit area. We find that waves traced to the ocean contribute only a very small amount of MF per unit area to the total whilst, consistent with our expectations from previous studies, the Southern Andes (grey) contribute the highest MF per unit area across all months. Small islands such as Kerguelen (brown) and South Georgia (yellow) contribute a disproportionately high percentage of observed MF per unit area. This is in agreement with Alexander and Grimsdell (2013) who carried out a comprehensive analysis of GW activity observed by AIRS over 14 islands in the Southern Ocean and concluded that including these island waves in climate models could contribute a significant fraction of the missing drag on Southern Hemisphere winds. Eckermann et al. (2016) studied the dynamics of orographic GWs observed in the mesosphere over the Aukland Islands (50.7°S 166.1°E) using the aircraft based Advanced Mesospheric Temperature Mapper (AMTM) concluding that orographic gravity wave drag due to subantarctic islands contributes significantly to the overall momentum budget and controlling the middle atmospheric dynamics. Our results here confirm the importance of MF generated due to these small islands and precisely quantify the MF values from each region.

Figure 10d shows that the Drake Passage region (light blue) contributes a much higher MF per unit area than the rest of the sea (blue). As discussed in Section 4.4, this is likely a combination of high-MF orographic events that have been mis-traced to the Drake Passage instead of the large sources of the Southern Andes and Antarctic Peninsula, non-orographic activity from storms in the Drake Passage region or orographic-jet induced gravity waves.

In Figure 10f we show momentum flux per unit area smoothed with a 7-day moving mean. Despite this smoothing, the strong intermittency of different sources can still be seen, in agreement with previous observational studies on intermittency (J. H. Jiang et al., 2002; Wright et al., 2013, 2017; Minamihara et al., 2020, and others). In particular, Kerguelen (brown), South Georgia (yellow) and New Zealand (red) exhibit seemingly-periodic activity, which may be related to lower-stratospheric planetary waves modulating gravity wave excitation and also influencing the visibility of these waves to AIRS. Vertical gravity wave propagation from tropospheric sources into the middle atmosphere over New Zealand was studied extensively during the DEEPWAVE campaign (for example, Fritts et al., 2016; Kaifler et al., 2015; Bramberger et al., 2017, and many others). Kaifler et al. (2015) carried out a detailed study of gravity wave activity over New Zealand using observations from the ground-based TELMA lidar (Temperature Lidar for Middle Atmosphere Research) during winter and spring 2014 (covering the DEEPWAVE campaign period). They found that GW activity over New Zealand was dominated by individual events of 1-3 days duration alternating with quieter periods, whilst in our results, momentum flux peaks in roughly 20 day periods, this is possibly due to observational filter effects with different instruments seeing different parts of the GW spectrum.

Finally, we quantify the contribution of momentum flux from the different regions in Table 1. This shows the percentage of total observed monthly MF attributed to each region. On average, 55.7 % of absolute MF traces back to land, while 44.3 % is traced back to the ocean. This means that whilst orographic sources contribute much more MF per unit area and as a result appear as hotspots of activity, non-orographic GW activity contributes more to the overall observed MF. This proportion varies temporally, with orographic sources contributing as much as 52.4% in May and as little as 34.6% in June to the total.

This is the first time that the relative contributions of these sources to the total observed momentum flux have been definitively quantified. For context, using stratosphere-level data only, Hindley et al. (2019) attributed 20-37% of the zonal momentum flux observed by AIRS between 68-35°S to the Southern Andes throughout June, July and August by comparing the observed zonal total to the fraction observed in the 80-55°W longitude range. Our work significantly expands upon this both by by employing ray-tracing methods to push the calculation back from the stratosphere to the source level and by quantifying all plausible source regions contributing to this belt. The Southern Andes, as expected, is the largest land source and contributes 10.1%-30.8%, then next strongest are the East Antarctic region (5.8%–17.4%) and the Transantarctic region (0.9%–10.9%). The large range on each of these values represents the significant seasonal variability at play: the Antarctic Peninsula contributes the same to the total observed MF on average as the Transantarctic region (6.1%) but with a much more consistent range (3.2%-7.8%). Kerguelen's contributes 0.1%–1.6% to the monthly average, with New Zealand just behind at 0%–0.7%. This zero lower bound is because in September there was almost no contribution to the total observed momentum flux, most likely due to the positioning of the jet away from New Zealand in that month. Finally, South Georgia and Australia contribute 0.3%–0.7% and 0.1%–0.9% across the winter months.

5 Conclusions

In this work, we have backwards ray-traced all AIRS polar winter observations of GWs over Antarctica and the surrounding area for the period May - September 2012. AIRS is sensitive to gravity waves long vertical wavelength waves which carry the majority of momentum flux. We use these 14.2 million traced waves to systematically explore the meridional propagation and downstream propagation of waves from key orographic regions. Examine the spatial split between orographically and non-orographically generated waves, and, for the first time, explicitly quantify the contributions of different source regions to the overall observed momentum flux. Our key conclusions are:

- Waves converge to 60°S at all longitudes, and not just over the Andes and Antarctic Peninsula. We measure an average meridional propagation distance $\sim$ 500 km from tropospheric sources to $\sim$40 km of altitude.
- Waves observed thousands of kilometres downstream of the Southern Andes, Antarctic Peninsula, Transantarctic Mountains, Prince Charles Mountains, Kerguelen, South Georgia and New Zealand can be traced back to distant sources. Such downstream propagation of these orographic waves is highly dependent on the background stratospheric wind, partly due to the strong winds of the jet refracting the waves to longer vertical wavelengths and increasing their observability to AIRS.
- Of those waves which trace back to sources over the ocean, we see a pattern dominated by strong non-orographic GW activity at all longitudes around 60°S except for the region between $\approx$ 20°W and $\approx$ 10°E. In future work with this dataset we will specifically investigate the role non-orographic sources in the southern polar region.
- We quantify the proportion of observed MF that is traced back to different regions (see Table 1). On average, orographic sources contribute 44 % and non-orographic sources 56 %. Land covers less than a quarter of this region, and thus it is likely that orographic-source waves contribute almost three times as much MF per unit area, but this is counterbalanced by the much larger area available for non-orographic sources to act. The measured values vary significantly by month.
- The small islands of Kerguelen and South Georgia contribute strongly to total overall MF observed despite only making up $<$ 1 % of the land area. In May, Kerguelen was responsible for 1.6 % of the overall observed MF in the stratosphere, and this contribution is likely to be even higher at shorter timescales due to the intermittency of these island sources.

Our work provides strong observational evidence of GW behaviour across the winter Southern Hemisphere and quantifies the propagation and momentum fluxes from different sources to aid future GW parametrisations.

Open Research Section

The 3-D AIRS temperature retrieval used in this work is described in (Hoffmann & Alexander, 2009) and is publicly available at (Hoffmann, 2021). ERA5 reanalysis used is also publicly available (Copernicus Climate Change Service, 2017).

Acknowledgments

This study is supported by the UK Natural Environment Research Council (NERC) under grant numbers NE/W003201/1(PN, CW and NH), NE/W003317/1(TMG), NE/S00985X/1(NH and CW). NH is supported by a NERC Independent Research Fellowship NE/X0178.

CW is also supported by NERC grant NE/V01837X/1 as well as a Royal Society University Research Fellowship URF/R/221023, Royal Society grants RGF/EA/180217 and RF/ERE/210079. PN is supported by a NERC GW4+ Doctoral Training Partnership studentship (NE/S007504/1). PB is supported by a University of Bath studentship. The authors gratefully acknowledge the University of Bath's Research Computing Group (doi.org/10.15125/b6cd-s854) for their support in this work.

References

Alexander, M. J. (1998, APR). Interpretations of observed climatological patterns in stratospheric gravity wave variance. *Journal of Geophysical Research: Atmospheres*, *103*(D8), 8627–8640. doi: 10.1029/97jd03325

Alexander, M. J., & Barnet, C. (2007). Using satellite observations to constrain parameterizations of gravity wave effects for global models. *J. Atmos. Sci.*, *64*, 1652–1665. doi: 10.1175/JAS3897.1

Alexander, M. J., Eckermann, S. D., Broutman, D., & Ma, J. (2009). Momentum flux estimates for South Georgia Island mountain waves in the stratosphere observed via satellite. *Geophy. Res. Lett.*, *36*, L12816. doi: 10.1029/2009GL038587

Alexander, M. J., Geller, M., McLandress, C., Polavarapu, S., Preusse, P., Sassi, F., ... Watanabe, S. (2010, JUL). Recent developments in gravity-wave effects in climate models and the global distribution of gravity-wave momentum flux from observations and models. *Quart. J. Roy. Meteor. Soc.*, *136*(650, A), 1103-1124. doi: {10.1002/qj.637}

Alexander, M. J., Gille, J., Cavanaugh, C., Coffey, M., Craig, C., Eden, T., ... Dean, V. (2008, May). Global estimates of gravity wave momentum flux from high resolution dynamics limb sounder observations. *Journal of Geophysical Research*, *113*(D15), 0148-0227. Retrieved from `https://doi.org/10.1029/2007jd008807` doi: 10.1029/2007jd008807

Alexander, M. J., & Grimsdell, A. W. (2013). Seasonal cycle of orographic gravity wave occurrence above small islands in the Southern Hemisphere: Implications for effects on the general circulation. *J. Geophys. Res.*, *118*, 11589–11599. doi: 10.1002/2013JD020526

Aumann, H., Chahine, M., Gautier, C., Goldberg, M., Kalnay, E., McMillin, L., ... Susskind, J. (2003, Feb). Airs/amsu/hsb on the aqua mission: design, science objectives, data products, and processing systems. *IEEE Transactions on Geoscience and Remote Sensing*, *41*(2), 253-264. doi: 10.1109/TGRS.2002.808356

Bacmeister, J. T., & Schoeberl, M. R. (1989). Breakdown of Vertically Propagating Two-Dimensional Gravity Waves Forced by Orography. *J. Atmos. Sci.*, *46*, 2109-2134.

Banyard, T. P., Wright, C. J., Hindley, N. P., Halloran, G., Krisch, I., Kaifler, B., & Hoffmann, L. (2021). Atmospheric gravity waves in aeolus wind lidar observations. *Geophysical Research Letters*, *48*(10), e2021GL092756. (e2021GL092756 2021GL092756) doi: https://doi.org/10.1029/2021GL092756

Bramberger, M., Dörnbrack, A., Bossert, K., Ehard, B., Fritts, D. C., Kaifler, B., ... Witschas, B. (2017). Does strong tropospheric forcing cause large-amplitude mesospheric gravity waves? a deepwave case study. *J. Geophys. Res.*, *122*(21), 11,422-11,443. doi: 10.1002/2017JD027371

Chahine, M. T., Pagano, T. S., Aumann, H. H., Atlas, R., Barnet, C., Bblaisdell, J., ... Zhou, L. (2006, 07). AIRS: Improving Weather Forecasting and Providing New Data on Greenhouse Gases. *Bulletin of the American Meteorological Society*, *87*(7), 911-926. doi: 10.1175/BAMS-87-7-911

Copernicus Climate Change Service. (2017). *ERA5: Fifth generation of ECMWF atmospheric reanalyses of the global climate.* European Centre For Medium-

Range Weather Forecasts (ECMWF), https://cds.climate.copernicus.eu/. ([Accessed March 2023])

Dunkerton, T. J. (1984, 12). Inertia–Gravity Waves in the Stratosphere. *Journal of the Atmospheric Sciences*, *41*(23), 3396-3404. doi: 10.1175/1520-0469(1984)041⟨3396:IWITS⟩2.0.CO;2

Eckermann, S. D., Broutman, D., Ma, J., Doyle, J. D., Pautet, P.-D., Taylor, M. J., ... Smith, R. B. (2016, OCT). Dynamics of orographic gravity waves observed in the mesosphere over the Auckland Islands during the deep propagating gravity wave experiment (DEEPWAVE). *J. Atmos. Sci.*, *73*(10), 3855-3876. doi: 10.1175/JAS-D-16-0059.1

Eckermann, S. D., & Marks, C. J. (1997). Grograt: A new model of the global propagation and dissipation of atmospheric gravity waves. *Advances in Space Research*, *20*(6), 1253-1256. Retrieved from https://www.sciencedirect.com/science/article/pii/S0273117797007801 (Coupling and Energetics in the Stratosphere-Mesosphere-Thermosphere- Ionosphere System) doi: https://doi.org/10.1016/S0273-1177(97)00780-1

Eckermann, S. D., & Preusse, P. (1999). Global Measurements of Stratospheric Mountain Waves from Space. *Science*, *286*, 1534–1537. doi: 10.1126/science.286.5444.1534

Eichinger, R., Rhode, S., Garny, H., Preusse, P., Pisoft, P., Kuchař, A., ... Kern, B. (2023). Emulating lateral gravity wave propagation in a global chemistry–climate model (emac v2.55.2) through horizontal flux redistribution. *Geoscientific Model Development*, *16*(19), 5561–5583. Retrieved from https://gmd.copernicus.org/articles/16/5561/2023/ doi: 10.5194/gmd-16-5561-2023

Ern, M., Preusse, P., Alexander, M. J., & Warner, C. D. (2004). Absolute values of gravity wave momentum flux derived from satellite data. *J. Geophys. Res.*, *109*, D20103. doi: 10.1029/2004JD004752

Ern, M., Trinh, Q. T., Preusse, P., Gille, J. C., Mlynczak, M. G., III, J. M. R., & Riese, M. (2018, April). GRACILE: a comprehensive climatology of atmospheric gravity wave parameters based on satellite limb soundings. *Earth System Science Data*, *10*(2), 857–892. doi: 10.5194/essd-10-857-2018

Fritts, D. C., & Alexander, M. J. (2003). Gravity wave dynamics and effects in the middle atmosphere. *Reviews of Geophysics*, *41*, 1003. doi: 10.1029/2001RG000106

Fritts, D. C., Riggin, D. M., Balsley, B. B., & Stockwell, R. G. (1998). Recent results with an mf radar at mcmurdo, antarctica: Characteristics and variability of motions near 12-hour period in the mesosphere. *Geophy. Res. Lett.*, *25*(3), 297–300. doi: 10.1029/97GL03702

Fritts, D. C., Smith, R. B., Taylor, M. J., Doyle, J. D., Eckermann, S. D., Dörnbrack, A., ... Ma, J. (2016). The deep propagating gravity wave experiment (deepwave): An airborne and ground-based exploration of gravity wave propagation and effects from their sources throughout the lower and middle atmosphere. *Bulletin of the American Meteorological Society*, *97*(3), 425 - 453. Retrieved from https://journals.ametsoc.org/view/journals/bams/97/3/bams-d-14-00269.1.xml doi: 10.1175/BAMS-D-14-00269.1

Garcia, R. R., Smith, A. K., Kinnison, D. E., de la Camara, A., & Murphy, D. J. (2017). Modification of the gravity wave parameterization in the whole atmosphere community climate model: Motivation and results. *Journal of the Atmospheric Sciences*, *74*(1), 275-291. doi: 10.1175/JAS-D-16-0104.1

Garfinkel, C. I., & Oman, L. D. (2018). Effect of gravity waves from small islands in the southern ocean on the southern hemisphere atmospheric circulation. *Journal of Geophysical Research: Atmospheres*, *123*(3), 1552-1561. doi: 10.1002/2017JD027576

Geldenhuys, M., Preusse, P., Krisch, I., Zülicke, C., Ungermann, J., Ern, M., ...

Riese, M. (2021). Orographically induced spontaneous imbalance within the jet causing a large-scale gravity wave event. *Atmos. Chem. Phys.*. doi: 10.5194/acp-21-10393-2021

Geller, M., Alexander, M. J., Love, P., Bacmeister, J., Ern, M., Hertzog, A., ... Zhou, T. (2013). A Comparison between Gravity Wave Momentum Fluxes in Observations and Climate Models. *Journal of Climate*, *26*, 6383–6405. doi: 10.1175/JCLI-D-12-00545.1

Green, B., Sheshadri, A., Alexander, M. J., Bramberger, M., & Lott, F. (2024). Gravity wave momentum fluxes estimated from project loon balloon data. *Journal of Geophysical Research: Atmospheres*, *129*(5), e2023JD039927. Retrieved from `https://agupubs.onlinelibrary.wiley.com/doi/abs/10.1029/2023JD039927` (e2023JD039927 2023JD039927) doi: https://doi.org/10.1029/2023JD039927

Hasha, A., Bühler, O., & Scinocca, J. (2008). Gravity wave refraction by three-dimensionally varying winds and the global transport of angular momentum. *Journal of the Atmospheric Sciences*, *65*(9), 2892 - 2906. Retrieved from `https://journals.ametsoc.org/view/journals/atsc/65/9/2007jas2561.1.xml` doi: 10.1175/2007JAS2561.1

Hendricks, E., Doyle, J., Eckermann, S. D., Jiang, Q., & Reinecke, P. (2014). What Is the Source of the Stratospheric Gravity Wave Belt in Austral Winter? *J. Atmos. Sci.*, *71*, 1583–1592. doi: 10.1175/JAS-D-13-0332.1

Hersbach, H., Bell, B., Berrisford, P., Hirahara, S., Horányi, A., Muñoz-Sabater, J., ... others (2020). The era5 global reanalysis. *Quarterly Journal of the Royal Meteorological Society*, *146*(730), 1999–2049.

Hertzog, A., Alexander, M. J., & Plougonven, R. (2012). On the Intermittency of Gravity Wave Momentum Flux in the Stratosphere. *J. Atmos. Sci.*, *69*, 3433–3448. doi: 10.1175/JAS-D-12-09.1

Hertzog, A., Boccara, G., Vincent, R. A., Vial, F., & Cocquerez, P. (2008). Estimation of gravity wave momentum flux and phase speeds from quasi-Lagrangian stratospheric balloon flights. Part II: Results from the Vorcore campaign in Antarctica. *J. Atmos. Sci.*, *65*, 3056–3070. doi: 10.1175/2008JAS2710.1

Hindley, N. P., Smith, N. D., Wright, C. J., Rees, D. A. S., & Mitchell, N. J. (2016, June). A two-dimensional stockwell transform for gravity wave analysis of AIRS measurements. *Atmospheric Measurement Techniques*, *9*(6), 2545–2565. doi: 10.5194/amt-9-2545-2016

Hindley, N. P., Wright, C. J., Gadian, A. M., Hoffmann, L., Hughes, J. K., Jackson, D. R., ... Ross, A. N. (2021). Stratospheric gravity waves over the mountainous island of south georgia: testing a high-resolution dynamical model with 3-d satellite observations and radiosondes. *Atmospheric Chemistry and Physics*, *21*(10), 7695–7722. Retrieved from `https://acp.copernicus.org/articles/21/7695/2021/` doi: 10.5194/acp-21-7695-2021

Hindley, N. P., Wright, C. J., Hoffmann, L., Moffat-Griffin, T., & Mitchell, N. J. (2020, November). An 18-year climatology of directional stratospheric gravity wave momentum flux from 3-d satellite observations. *Geophysical Research Letters*, *47*(22), e2020GL089557. doi: 10.1029/2020gl089557

Hindley, N. P., Wright, C. J., Smith, N. D., Hoffmann, L., Holt, L. A., Alexander, M. J., ... Mitchell, N. J. (2019). Gravity waves in the winter stratosphere over the southern ocean: high-resolution satellite observations and 3-d spectral analysis. *Atmospheric Chemistry and Physics*, *19*(24), 15377–15414. doi: 10.5194/acp-19-15377-2019

Hindley, N. P., Wright, C. J., Smith, N. D., & Mitchell, N. J. (2015). The southern stratospheric gravity wave hot spot: individual waves and their momentum fluxes measured by cosmic gps-ro. *Atmos. Chem. Phys.*, *15*(14), 7797–7818. doi: 10.5194/acp-15-7797-2015

Hoffmann, L. (2021). *Airs/aqua observations of gravity waves [dataset].* doi: 10

.26165/JUELICH-DATA/LQAAJA

Hoffmann, L., & Alexander, M. J. (2009). Retrieval of stratospheric temperatures from Atmospheric Infrared Sounder radiance measurements for gravity wave studies. *J. Geophys. Res.*, *114*, D07105. doi: 10.1029/2008JD011241

Hoffmann, L., Alexander, M. J., Clerbaux, C., Grimsdell, A. W., Meyer, C. I., Roessler, T., & Tournier, B. (2014). Intercomparison of stratospheric gravity wave observations with AIRS and IASI. *Atmos. Meas. Tech.*, *7*(12), 4517-4537. doi: {10.5194/amt-7-4517-2014}

Hoffmann, L., Grimsdell, A. W., & Alexander, M. J. (2016). Stratospheric gravity waves at southern hemisphere orographic hotspots: 2003–2014 airs/aqua observations. *Atmos. Chem. Phys.*, *16*(14), 9381–9397. doi: 10.5194/acp-16-9381-2016

Hoffmann, L., Xue, X., & Alexander, M. J. (2013). A global view of stratospheric gravity wave hotspots located with Atmospheric Infrared Sounder observations. *J. Geophys. Res.*, *118*, 416–434. doi: 10.1029/2012JD018658

Holt, L. A., Alexander, M. J., Coy, L., Liu, C., Molod, A., Putman, W., & Pawson, S. (2017). An evaluation of gravity waves and gravity wave sources in the southern hemisphere in a 7km global climate simulation. *Quarterly Journal of the Royal Meteorological Society*, *143*(707), 2481-2495. doi: 10.1002/qj.3101

Holt, L. A., Brabec, C. M., & Alexander, M. J. (2023). Exploiting high-density zonal-sampling of hirdls profiles near 60°s to investigate missing drag in chemistry-climate models. *Journal of Geophysical Research: Atmospheres*, *128*(8), e2022JD037398. Retrieved from `https://agupubs.onlinelibrary.wiley.com/doi/abs/10.1029/2022JD037398` (e2022JD037398 2022JD037398) doi: https://doi.org/10.1029/2022JD037398

Jewtoukoff, V., Hertzog, A., Plougonven, R., de la Camara, A., & Lott, F. (2015). Comparison of gravity waves in the southern hemisphere derived from balloon observations and the ecmwf analyses. *Journal of the Atmospheric Sciences*, *72*(9), 3449-3468. doi: 10.1175/JAS-D-14-0324.1

Jiang, J. H., Wu, D. L., & Eckermann, S. D. (2002). Upper atmosphere research satellite (uars) mls observation of mountain waves over the andes. *Journal of Geophysical Research: Atmospheres*, *107*(D20), SOL 15-1-SOL 15-10. doi: 10.1029/2002JD002091

Jiang, Q., Doyle, J. D., Eckermann, S. D., & Williams, B. P. (2019). Stratospheric trailing gravity waves from new zealand. *Journal of the Atmospheric Sciences*, *76*(6), 1565 - 1586. Retrieved from `https://journals.ametsoc.org/view/journals/atsc/76/6/jas-d-18-0290.1.xml` doi: 10.1175/JAS-D-18-0290.1

Kaifler, B., Kaifler, N., Ehard, B., Dörnbrack, A., Rapp, M., & Fritts, D. C. (2015, November). Influences of source conditions on mountain wave penetration into the stratosphere and mesosphere. *Geophysical Research Letters*, *42*(21), 9488–9494. doi: 10.1002/2015gl066465

Krasauskas, L., Kaifler, B., Rhode, S., Ungermann, J., Woiwode, W., & Preusse, P. (2023). Oblique propagation and refraction of gravity waves over the andes observed by gloria and alima during the southtrac campaign. *Journal of Geophysical Research: Atmospheres*, *128*(10), e2022JD037798. Retrieved from `https://agupubs.onlinelibrary.wiley.com/doi/abs/10.1029/2022JD037798` (e2022JD037798 2022JD037798) doi: https://doi.org/10.1029/2022JD037798

Krisch, I., Preusse, P., Ungermann, J., Dörnbrack, A., Eckermann, S. D., Ern, M., … Riese, M. (2017). First tomographic observations of gravity waves by the infrared limb imager gloria. *Atmospheric Chemistry and Physics*, *17*(24), 14937–14953. doi: 10.5194/acp-17-14937-2017

Lighthill, M. J. (1967). Waves in fluids. *Communications on Pure and Applied Mathematics*, *20*(2), 267-293. Retrieved from `https://onlinelibrary.wiley.com/doi/abs/10.1002/cpa.3160200204` doi: https://doi.org/10.1002/cpa

.3160200204

Marks, C. J., & Eckermann, S. D. (1995). A three-dimensional nonhydrostatic ray-tracing model for gravity waves: Formulation and preliminary results for the middle atmosphere. *Journal of the Atmospheric Sciences*, *52*(11), 1959-1984. doi: 10.1175/1520-0469(1995)052⟨1959:ATDNRT⟩2.0.CO;2

McDonald, A. J. (2012). Gravity wave occurrence statistics derived from paired COSMIC/FORMOSAT3 observations. *J. Geophys. Res.*, *117*, D15106. doi: 10.1029/2011JD016715

McLandress, C., Shepherd, T. G., Polavarapu, S., & Beagley, S. R. (2012). Is Missing Orographic Gravity Wave Drag near 60°S the Cause of the Stratospheric Zonal Wind Biases in Chemistry–Climate Models? *J. Atmos. Sci.*, *69*, 802–818. doi: 10.1175/JAS-D-11-0159.1

McLandress, C., Shepherd, T. G., Scinocca, J. F., Plummer, D. A., Sigmond, M., Jonsson, A. I., & Reader, M. C. (2011). Separating the dynamical effects of climate change and ozone depletion. part ii: Southern hemisphere troposphere. *Journal of Climate*, *24*(6), 1850-1868. doi: 10.1175/2010JCLI3958.1

Minamihara, Y., Sato, K., & Tsutsumi, M. (2020). Intermittency of gravity waves in the antarctic troposphere and lower stratosphere revealed by the pansy radar observation. *Journal of Geophysical Research: Atmospheres*, *125*(15), e2020JD032543. Retrieved from `https://agupubs.onlinelibrary.wiley.com/doi/abs/10.1029/2020JD032543` (e2020JD032543 2020JD032543) doi: https://doi.org/10.1029/2020JD032543

Moffat-Griffin, T., Colwell, S. R., Wright, C. J., Hindley, N. P., & Mitchell, N. J. (2020). Radiosonde observations of a wintertime meridional convergence of gravity waves around 60°s in the lower stratosphere. *Geophysical Research Letters*, *47*(20), e2020GL089740. doi: https://doi.org/10.1029/2020GL089740

Perrett, J., Wright, C. J., Hindley, N. P., Hoffmann, L., Mitchell, N. J., Preusse, P., . . . S., E. (2020). Determining gravity wave sources and propagation in the southern hemisphere by ray-tracing airs measurements. *Geophysical Research Letters*. doi: 10.1029/2020GL088621

Plougonven, R., de la Cámara, A., Hertzog, A., & Lott, F. (2020). How does knowledge of atmospheric gravity waves guide their parameterizations? *Quarterly Journal of the Royal Meteorological Society*, *146*(728), 1529-1543. doi: 10.1002/qj.3732

Plougonven, R., Hertzog, A., & Guez, L. (2013). Gravity waves over Antarctica and the Southern Ocean: consistent momentum fluxes in mesoscale simulations and stratospheric balloon observations. *Quart. J. Roy. Meteor. Soc.*, *139*, 101–118. doi: 10.1002/qj.1965

Plougonven, R., Jewtoukoff, V., de la Cámara, A., Lott, F., & Hertzog, A. (2017). On the relation between gravity waves and wind speed in the lower stratosphere over the southern ocean. *Journal of the Atmospheric Sciences*, *74*(4), 1075-1093. doi: 10.1175/JAS-D-16-0096.1

Pramitha, M., Kumar, K. K., Ratnam, M. V., Praveen, M., & Rao, S. V. B. (2020). Gravity wave source spectra appropriation for mesosphere lower thermosphere using meteor radar observations and grograt model simulations. *Geophysical Research Letters*, *47*(19), e2020GL089390. Retrieved from `https://agupubs.onlinelibrary.wiley.com/doi/abs/10.1029/2020GL089390` (e2020GL089390 2020GL089390) doi: https://doi.org/10.1029/2020GL089390

Preusse, P., Dörnbrack, A., & Eckermann, S. (2002). Space-based measurements of stratospheric mountain waves by CRISTA 1. Sensitivity, analysis method, and a case study. *J. Geophys. Res.*, *107*, 8178. doi: 10.1029/2001JD000699

Preusse, P., Eckermann, S. D., Ern, M., Oberheide, J., Picard, R. H., Roble, R. G., . . . Mlynczak, M. G. (2009). Global ray tracing simulations of the saber gravity wave climatology. *Journal of Geophysical Research: Atmospheres*, *114*(D8). Retrieved from `https://agupubs.onlinelibrary.wiley.com/doi/`

abs/10.1029/2008JD011214 doi: https://doi.org/10.1029/2008JD011214

Preusse, P., Ern, M., Bechtold, P., Eckermann, S. D., Kalisch, S., Trinh, Q. T., & Riese, M. (2014). Characteristics of gravity waves resolved by ECMWF. *Atmos. Chem. Phys.*, *14*. doi: 10.5194/acp-14-10483-2014

Pulido, M., Rodas, C., Dechat, D., & Lucini, M. M. (2013). High gravity-wave activity observed in patagonia, southern america: generation by a cyclone passage over the andes mountain range. *Quarterly Journal of the Royal Meteorological Society*, *139*(671), 451-466. Retrieved from https://rmets.onlinelibrary.wiley.com/doi/abs/10.1002/qj.1983 doi: https://doi.org/10.1002/qj.1983

Rapp, M., Kaifler, B., Dörnbrack, A., Gisinger, S., Mixa, T., Reichert, R., ... Engel, A. (2021). Southtrac-gw: An airborne field campaign to explore gravity wave dynamics at the world's strongest hotspot. *Bulletin of the American Meteorological Society*, *102*(4), E871 - E893. Retrieved from https://journals.ametsoc.org/view/journals/bams/102/4/BAMS-D-20-0034.1.xml doi: 10.1175/BAMS-D-20-0034.1

Rhode, S., Preusse, P., Ern, M., Ungermann, J., Krasauskas, L., Bacmeister, J., & Riese, M. (2023). A mountain ridge model for quantifying oblique mountain wave propagation and distribution. *Atmospheric Chemistry and Physics*, *23*(14), 7901–7934. Retrieved from https://acp.copernicus.org/articles/23/7901/2023/ doi: 10.5194/acp-23-7901-2023

Sato, K., Tateno, S., Watanabe, S., & Kawatani, Y. (2011). Gravity Wave Characteristics in the Southern Hemisphere Revealed by a High-Resolution Middle-Atmosphere General Circulation Model. *J. Atmos. Sci.*, *69*, 1378–1396. doi: 10.1175/JAS-D-11-0101.1

Strube, C., Preusse, P., Ern, M., & Riese, M. (2021). Propagation paths and source distributions of resolved gravity waves in ecmwf-ifs analysis fields around the southern polar night jet. *Atmospheric Chemistry and Physics Discussions*, *2021*, 1–39. doi: 10.5194/acp-2021-160

Vosper, S. B. (2015). Mountain waves and wakes generated by south georgia: implications for drag parametrization. *QJRMS*, *141*(692), 2813-2827. doi: 10.1002/qj.2566

Watanabe, S., Kawatani, Y., Tomikawa, Y., Miyazaki, K., Takahashi, M., & Sato, K. (2008). General aspects of a T213L256 middle atmosphere general circulation model. *J. Geophys. Res.*, *113*, D12110. doi: 10.1029/2008JD010026

Watanabe, S., Sato, K., & Takahashi, M. (2006). A general circulation model study of the orographic gravity waves over antarctica excited by katabatic winds. *Journal of Geophysical Research: Atmospheres*, *111*(D18). Retrieved from https://agupubs.onlinelibrary.wiley.com/doi/abs/10.1029/2005JD006851 doi: https://doi.org/10.1029/2005JD006851

Wrasse, C. M., Nakamura, T., Takahashi, H., Medeiros, A. F., Taylor, M. J., Gobbi, D., ... Admiranto, A. G. (2006). Mesospheric gravity waves observed near equatorial and low-middle latitude stations: wave characteristics and reverse ray tracing results. *Annales Geophysicae*, *24*(12), 3229–3240. Retrieved from https://angeo.copernicus.org/articles/24/3229/2006/ doi: 10.5194/angeo-24-3229-2006

Wright, C. J., & Gille, J. C. (2013). Detecting overlapping gravity waves using the S-Transform. *Geophy. Res. Lett.*, *40*, 1850–1855. doi: 10.1002/grl.50378

Wright, C. J., Hindley, N. P., Alexander, M. J., Holt, L. A., & Hoffmann, L. (2021). Using vertical phase differences to better resolve 3d gravity wave structure. *Atmospheric Measurement Techniques*, *14*(9), 5873–5886. Retrieved from https://amt.copernicus.org/articles/14/5873/2021/ doi: 10.5194/amt-14-5873-2021

Wright, C. J., Hindley, N. P., Hoffmann, L., Alexander, M. J., & Mitchell, N. J. (2017). Exploring gravity wave characteristics in 3-d using a novel s-transform technique: Airs/aqua measurements over the southern andes and drake passage. *Atmospheric Chemistry and Physics*, *17*(13), 8553–8575. doi: 10.5194/acp-17-8553-2017

Wright, C. J., Hindley, N. P., Moss, A. C., & Mitchell, N. J. (2016). Multi-instrument gravity-wave measurements over tierra del fuego and the drake passage - part 1: Potential energies and vertical wavelengths from airs, cosmic, hirdls, mls-aura, saamer, saber and radiosondes. *Atmospheric Measurement Techniques*, *9*(3), 877–908. doi: 10.5194/amt-9-877-2016

Wright, C. J., Osprey, S. M., & Gille, J. C. (2013). Global observations of gravity wave intermittency and its impact on the observed momentum flux morphology. *J. Geophys. Res.*, *118*, 10,980–10,993. doi: 10.1002/jgrd.50869

Wu, D. L. (2004). Mesoscale gravity wave variances from amsu-a radiances. *Geophy. Res. Lett.*, *31*(12), 1944-8007. (L12114) doi: 10.1029/2004GL019562

Wu, D. L., & Eckermann, S. D. (2008). Global gravity wave variances from aura mls: Characteristics and interpretation. *Journal of the Atmospheric Sciences*, *65*(12), 3695-3718. doi: 10.1175/2008JAS2489.1